CO₂ migration in saline aquifers. Part 2. Capillary and solubility trapping

C. W. MacMinn[1], M. L. Szulczewski[2] and R. Juanes[2]†

[1] Department of Mechanical Engineering, Massachusetts Institute of Technology, Cambridge, MA 02139, USA

[2] Department of Civil and Environmental Engineering, Massachusetts Institute of Technology, Cambridge, MA 02139, USA

The large-scale injection of carbon dioxide (CO_2) into saline aquifers is a promising tool for reducing atmospheric CO_2 emissions to mitigate climate change. An accurate assessment of the post-injection migration and trapping of the buoyant plume of CO_2 is essential for estimates of storage capacity and security, but these physical processes are not fully understood. In Part 1 of this series, we presented a complete solution to a theoretical model for the migration and capillary trapping of a plume of CO_2 in a confined, sloping aquifer with a natural groundwater through-flow. Here, we incorporate solubility trapping, where CO_2 from the buoyant plume dissolves into the ambient brine via convective mixing. We develop semi-analytical solutions to the model in two limiting cases: when the water beneath the plume saturates with dissolved CO_2 very slowly or very quickly ('instantaneously') relative to plume motion. We show that solubility trapping can greatly slow the speed at which the plume advances, and we derive an explicit analytical expression for the position of the nose of the plume as a function of time. We then study the competition between capillary and solubility trapping, and the impact of solubility trapping on the storage efficiency, a macroscopic measure of plume migration. We show that solubility trapping can increase the storage efficiency by several-fold, even when the fraction of CO_2 trapped by solubility trapping is small.

Key words: gravity currents, porous media

1. Introduction

Mitigation of climate change will necessitate a reduction in atmospheric carbon dioxide (CO_2) emissions; however, electric power generation is a primary source of CO_2 emissions, and demand for electric power is expected to rise steadily for the foreseeable future. The global transition to a low-carbon energy infrastructure will take tens to hundreds of years. One promising tool for reducing CO_2 emissions during this transitional period is the large-scale injection of CO_2 into deep saline aquifers (Bachu, Gunter & Perkins 1994; Lackner 2003; Schrag 2007; Orr 2009).

At typical aquifer conditions, CO_2 is less dense and less viscous than the ambient groundwater, making it buoyant and mobile. As a result, a primary concern is the

† Email address for correspondence: juanes@mit.edu

risk of leakage into shallow formations through a pre-existing well or fracture, or via the activation of a fault. An accurate assessment of the post-injection migration and trapping of the CO_2 is essential for estimates of storage capacity and security, but many of the relevant physical processes are not fully understood. In Part 1 of this series (MacMinn, Szulczewski & Juanes 2010), we developed a complete solution to a hyperbolic gravity current model for CO_2 migration in a confined, tilted aquifer with a natural groundwater through-flow. We included capillary trapping, where small blobs of CO_2 are immobilized by capillarity at the trailing edge of the plume, and also the tongued end-of-injection plume shape. We showed that the migration behaviour depends strongly on the mobility ratio, the amount of capillary trapping, and the importance of aquifer slope relative to groundwater flow. We explored the effect of these parameters on the overall storage efficiency, a measure of the fraction of the aquifer pore space that can be used to store CO_2, and we showed that the interplay between groundwater flow and aquifer slope can change the storage efficiency by a factor of two to five. In particular, we found that the maximum efficiency is achieved in sloping aquifers with a moderate down-dip groundwater flow, conditions which are known to occur in many continental sedimentary basins (Garven 1995).

We did not consider solubility trapping in Part 1, but CO_2 is weakly soluble in groundwater and both residual and mobile CO_2 will dissolve slowly into the nearby groundwater as the plume migrates. Dissolved CO_2 is considered trapped because it is no longer buoyant: water with dissolved CO_2 is denser than either water or free-phase CO_2. As a result, the boundary layer of CO_2-saturated groundwater near the mobile plume is unstable, and this unstable density stratification eventually results in so-called convective mixing, where fingers of dense, CO_2-rich groundwater sink away from the interface as fingers of fresh groundwater rise upward.

The convective-mixing instability has been studied in various contexts. For example, Elder (1968) considered heat transfer in a porous medium heated from below, and Wooding, Tyler & White (1997a) and Wooding *et al.* (1997b) considered salt transport in a porous medium with a salt source at the top. The implications of this process for geological CO_2 storage were first pointed out by Weir, White & Kissling (1996) and discussed by Lindeberg & Wessel-Berg (1997). Several studies have since investigated the onset of the instability for a stationary layer of CO_2 overlying water. Riaz *et al.* (2006) performed a linear stability analysis, and used high-resolution numerical simulations to study the early-time nonlinear development of the fingers. Ennis-King & Paterson (2005) and Ennis-King, Preston & Paterson (2005) showed that permeability anisotropy slows the onset of the instability, and Hidalgo & Carrera (2009) showed that hydrodynamic dispersion can speed the onset of the instability. Rapaka *et al.* (2008, 2009) studied the onset of the instability using non-modal stability theory, and used these techniques to investigate onset in the context of anisotropic and layered porous media. Slim & Ramakrishnan (2010) studied the onset of convective mixing in an aquifer of finite thickness, and explored two different types of boundary condition at the CO_2–water interface. In all cases, the onset time for convective mixing was found to be short relative to time scales of interest in geological CO_2 storage.

Ennis-King & Paterson (2005) showed by a simple scaling analysis that convective mixing dramatically increases the rate of solubility trapping compared to diffusive transport, and noted that the small-scale features of convective mixing would probably necessitate an upscaled model for solubility trapping at the basin scale. Pau *et al.* (2010) and Neufeld *et al.* (2010) used high-resolution numerical simulations to study macroscopic features of the convective-mixing process, showing that the time-averaged rate of CO_2 solubility trapping due to convective mixing is approximately constant.

Kneafsey & Pruess (2010), Neufeld *et al.* (2010), and Backhaus, Turitsyn & Ecke (2011) have confirmed this experimentally. By taking advantage of these results, an upscaled model for solubility trapping due to convective mixing can be incorporated into computational models for CO_2 migration at large scales (Gasda, Nordbotten & Celia 2011).

Here, we incorporate a simple upscaled model for solubility trapping into the theoretical migration model considered in Part 1. Such sharp-interface, gravity current models have been used recently to provide important insights into the injection (Nordbotten & Celia 2006; Neufeld, Vella & Huppert 2009; Gunn & Woods 2011), spreading (Bickle *et al.* 2007; Hesse *et al.* 2007; MacMinn & Juanes 2009), and migration (Hesse, Orr & Tchelepi 2008; Juanes, MacMinn & Szulczewski 2010; MacMinn *et al.* 2010) of CO_2 in saline aquifers. Here we study the importance of solubility trapping relative to capillary trapping during post-injection migration, and the impact of solubility trapping on the migration behaviour and the storage efficiency. We show that solubility trapping plays a major role in CO_2 migration, and can increase the storage efficiency by several-fold even when the volume dissolved is small.

In § 2, we review the model for CO_2 migration without solubility trapping. In § 3, we develop the model for solubility trapping due to convective mixing. In § 4, we present the model for CO_2 migration with solubility trapping. In § 5, we develop semi-analytical solutions to the model in some limiting cases. In § 6, we use the model and solutions to study the competition between capillary and solubility trapping, and their impact on migration.

2. Model for CO₂ migration

In Part 1 of this series, we derived a theoretical model for the migration and capillary trapping of a plume of CO_2 in a confined, sloping aquifer with a natural groundwater through-flow (Bear 1972; Kochina, Mikhailov & Filinov 1983; Huppert & Woods 1995; Hesse *et al.* 2008; Juanes *et al.* 2010; MacMinn *et al.* 2010). We review that model here.

We are interested in large CO_2 storage projects, because large quantities of CO_2 would need to be stored in order to significantly reduce atmospheric emissions. We therefore study the evolution of the CO_2 plume at the geologic-basin scale, as proposed by Nicot (2008) (figure 1). We take the aquifer to be homogeneous, with an arbitrary tilt relative to the horizontal and a net groundwater through-flow to the right. We assume line symmetry in the *y*-direction (figure 1). As a result, all volumes and fluxes discussed here are per-unit-length of the line-drive well array unless specifically noted otherwise. We take the fluids to be incompressible and Newtonian, with constant and uniform properties within the aquifer. We denote the CO_2 density and viscosity by ρ_g and μ_g, respectively, and the water density and viscosity by ρ_w and μ_w. We employ a sharp-interface approximation, neglecting saturation gradients as well as the capillary pressure. We further assume vertical equilibrium, neglecting the vertical component of the fluid velocity relative to the horizontal one. We divide the domain into three regions of uniform fluid saturation with sharp interfaces corresponding to saturation discontinuities (figure 2): Region 1 is the plume of mobile CO_2, containing free-phase CO_2 and a saturation S_{wc} of connate or residual groundwater; Region 2 is the region from which the plume has receded, containing mobile groundwater and a saturation S_{gr} of residual, free-phase CO_2; and Region 3 contains mobile groundwater with some dissolved CO_2, and no free-phase CO_2.
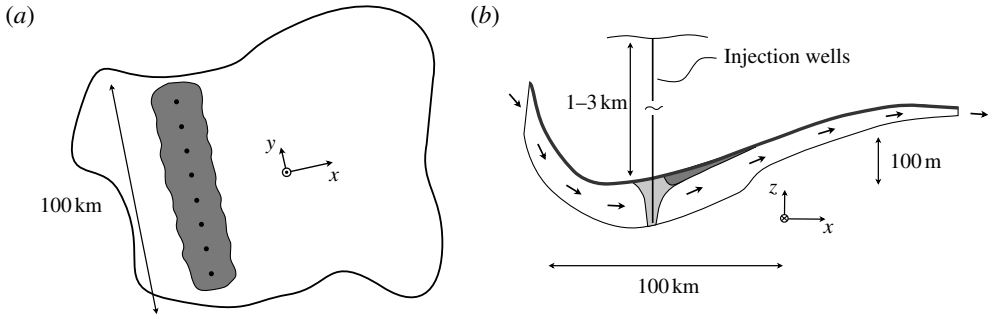
FIGURE 1. Large-scale geological storage of CO_2 requires injection at the scale of geologic basins. (*a*) A bird's-eye view of CO_2 injection into a saline aquifer via a linear or 'line-drive' array of wells. The plumes from the individual wells merge together as the CO_2 spreads away from the well array (black dots), and we model the single resulting plume (dark grey) as two-dimensional in the *x–z* plane, with some width *W* in the *y*-direction equal to the length of the well array. (*b*) A section view of post-injection CO_2 migration due to groundwater flow and/or slope. Residual CO_2 (light grey) is left behind, trapped, in the wake of the mobile plume (Juanes *et al.* 2006). Groundwater is shown in white, and the caprock as a thick line. Arrows indicate the direction of groundwater flow. Typical horizontal and vertical scales are indicated. The vertical scale of the aquifer is greatly exaggerated.
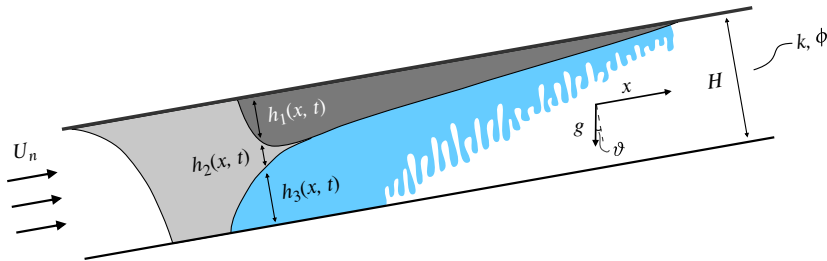

FIGURE 2. (Colour online available at journals.cambridge.org/flm) After injection stops, the plume of mobile CO_2 (dark grey) will migrate due to a combination of groundwater flow and aquifer slope, leaving residual CO_2 in its wake (light grey). CO_2 will dissolve from the plume by convective mixing, as indicated by the fingers of dense, CO_2-rich groundwater (blue) falling away from the plume. We divide the domain into three regions of uniform CO_2 and groundwater saturation, separated by sharp interfaces corresponding to saturation discontinuities: Region 1 (dark grey) contains mobile CO_2 and a saturation S_{wc} of connate (residual) groundwater; Region 2 (light grey) contains mobile groundwater and a saturation S_{gr} of residual CO_2; Region 3 (white, blue) contains mobile groundwater with some dissolved CO_2. The aquifer has a total thickness H, and the thickness of Region i, $i = 1, 2, 3$, is denoted $h_i(x, t)$. Groundwater flows naturally through the aquifer from left to right with velocity U_n; the aquifer has permeability k and porosity ϕ, as well as an arbitrary angle of tilt ϑ measured anticlockwise from the direction of gravity.

With the assumptions above, and neglecting solubility trapping, we can write the Darcy velocity for each fluid in each region and relate them through conservation of mass, accounting for the residual fluid that crosses each interface (Hesse, Tchelepi & Orr 2006; Hesse *et al.* 2008). The resulting conservation law for the local thickness of

the plume, $h_1(x, t)$, is

$$(1 - S_{wc})\phi\widetilde{\mathscr{R}}\frac{\partial h_1}{\partial t} + \frac{\partial F_g}{\partial x} = 0, \tag{2.1}$$

where

$$F_g(h_1(x, t)) = Qf + (1 - S_{wc})\phi\kappa \sin\vartheta (1 - f)h_1$$
$$- (1 - S_{wc})\phi\kappa \cos\vartheta (1 - f)h_1\frac{\partial h_1}{\partial x} \tag{2.2}$$

is the total horizontal flow of CO$_2$ through the plume at some position x and time t. The discontinuous accumulation coefficient $\widetilde{\mathscr{R}}$ captures the fact that residual CO$_2$ is lost from the plume due to capillary trapping by taking different values for drainage and imbibition,

$$\widetilde{\mathscr{R}} = \begin{cases} 1 & \text{if } \partial h_1/\partial t > 0 \text{ and } h_2 = 0, \\ 1 - \Gamma & \text{otherwise.} \end{cases} \tag{2.3}$$

The parameter $\Gamma = S_{gr}/(1 - S_{wc})$ is the capillary trapping number, which measures the amount of residual CO$_2$ that is left behind at the trailing edge of the plume and takes a constant value between zero (no capillary trapping) and one. A net volume rate Q of fluid flows through the aquifer from left to right. We denote the mobility of the mobile fluid in Region i, $i = 1, 2, 3$, by $\lambda_i = k_{ri}/\mu_i$, where k_{ri} and μ_i are the relative permeability to that fluid and the viscosity of that fluid, respectively. For simplicity, we neglect the reduction of water mobility due to the presence of residual CO$_2$ in region 2, taking $\lambda_2 = \lambda_3$, although this effect can be included (Juanes & MacMinn 2008). The nonlinear function $f(h_1)$ is then given by

$$f(h_1) = \frac{\lambda_1 h_1}{\lambda_1 h_1 + \lambda_3(H - h_1)}. \tag{2.4}$$

The characteristic buoyancy-driven velocity of the plume is

$$\kappa = \frac{\Delta\rho gk\lambda_1}{(1 - S_{wc})\phi}, \tag{2.5}$$

where $\Delta\rho = \rho_w - \rho_g$ is the density difference between the groundwater and the CO$_2$, g is the force per unit mass due to gravity, and k and ϕ are the intrinsic permeability and porosity of the aquifer, respectively.

The conservation law for the layer of water beneath the plume, which has total thickness $h_w = h_2 + h_3 = H - h_1$, is readily derived from conservation of mass or by rewriting (2.1) in terms of h_w. It can be written as

$$(1 - S_{wc})\phi\widetilde{\mathscr{R}}\frac{\partial h_w}{\partial t} + \frac{\partial F_w}{\partial x} = 0, \tag{2.6}$$

where

$$F_w(h_1(x, t)) = Q(1 - f) - (1 - S_{wc})\phi\kappa \sin\vartheta (1 - f)h_1$$
$$+ (1 - S_{wc})\phi\kappa \cos\vartheta (1 - f)h_1\frac{\partial h_1}{\partial x} \tag{2.7}$$

is the total horizontal flow of groundwater at position x and time t. Note that $F_g + F_w = Q$, the total horizontal flow of fluid through the aquifer. Equation (2.6)
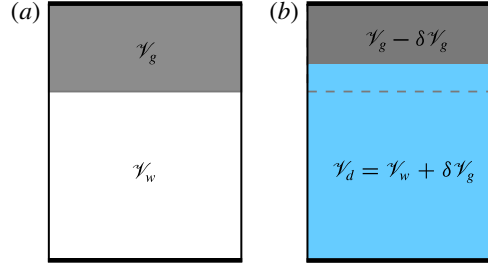
FIGURE 3. (Colour online) We assume that total fluid volume is conserved as CO_2 dissolves into groundwater. Consider (*a*) a closed box containing a volume $\mathcal{V}_g$ of free-phase CO_2 (dark grey) and a volume $\mathcal{V}_w$ of groundwater (white). We assume that a volume $\delta\mathcal{V}_g$ of the CO_2 then dissolves into the groundwater to form (*b*) a volume $\mathcal{V}_d = \mathcal{V}_w + \delta\mathcal{V}_g$ of groundwater with dissolved CO_2 (light grey (blue online)), and the total fluid volume within the box is unchanged. This assumption violates conservation of mass, introducing a relative error of size χ_v into the mass balance, but we adopt it for simplicity. To eliminate this error would require a complete treatment of the kinetics and thermodynamics of the CO_2–water system. The saturated volume fraction χ_v (3.1) is here $\chi_v = \delta\mathcal{V}_g/\mathcal{V}_d$.

is redundant since $h_w = H - h_1$, and we need only solve (2.1). However, (2.7) will be useful when solubility trapping is included (§ 3.4).

3. Model for solubility trapping due to convective mixing

We now consider solubility trapping of CO_2 from the mobile plume due to convective mixing. We denote by χ_m the maximum or saturated mass fraction of dissolved CO_2 in groundwater. We denote by ρ_d the density of groundwater containing mass fraction χ_m of dissolved CO_2. It is convenient here to work in terms of a volume fraction χ_v,

$$\chi_v = \rho_d \chi_m / \rho_g, \tag{3.1}$$

which measures the equivalent free-phase volume of CO_2 dissolved per unit volume of groundwater saturated with dissolved CO_2. The values of χ_m and χ_v depend strongly on the aquifer temperature and pressure, and on the salinity of the groundwater. Typical values of χ_v range from 0.03 to 0.1 (García 2001; Bachu 2003; Duan & Sun 2003; Kharaka & Hanor 2003; Carbon Capture and Sequestration Technologies @ MIT 2010). We take χ_v to be constant within a given aquifer.

We assume that total fluid volume is conserved as free-phase CO_2 dissolves into groundwater (figure 3). This assumption introduces a relative error in the mass balance of size χ_v, but we adopt it for simplicity. To eliminate this error would require a complete treatment of the kinetics and thermodynamics of the CO_2–water system.

3.1. *Onset time for convective mixing*

It has been shown from linear stability analysis (Ennis-King & Paterson 2005; Riaz *et al.* 2006; Pau *et al.* 2010) that the onset time for convective mixing can be written as

$$t_{onset} = \alpha_0 D_{eff} \left(\frac{\phi}{\Delta\rho_d g k \lambda_3} \right)^2, \tag{3.2}$$

where $\Delta\rho_d = \rho_d - \rho_w$ is the density difference that drives convective mixing and $\alpha_0 \sim 10^3$ is a dimensionless constant (Pau *et al.* 2010). D_{eff} is the effective

diffusion/dispersion coefficient for CO_2 in brine in the aquifer rock; velocity-dependent dispersion can speed the onset of the instability (Hidalgo & Carrera 2009), but is not included here. We compare this time to the time it would take the leading edge of the CO_2 plume to travel one characteristic length in the horizontal direction during migration due to groundwater flow or aquifer slope (Juanes & MacMinn 2008; Hesse *et al.* 2008; MacMinn *et al.* 2010),

$$t_{flow} = \frac{Q_i T_i/2}{\mathscr{M} U_n H}, \quad t_{slope} = \frac{Q_i T_i/2}{\Delta \rho g k \lambda_1 H \sin \vartheta}. \tag{3.3}$$

When $t_{onset}/t_{flow} \ll 1$ and $t_{onset}/t_{slope} \ll 1$, the onset time for convective mixing is negligible compared to typical migration time scales, meaning that convective mixing begins instantaneously along the entire plume in post-injection migration. We assume here that this is always the case.

3.2. *Rate of solubility trapping due to convective mixing*

We denote the upscaled mass flux of solubility trapping due to convective mixing by q_d^m. In principle, this flux is a function of the details of the complex convective flow beneath the plume. It is natural to expect that this flux should scale with the characteristic speed κ_d at which fingers of heavy water sink away from the plume,

$$\kappa_d = \frac{\Delta \rho_d g k \lambda_3}{\phi}, \tag{3.4}$$

and with the concentration of CO_2 carried by those fingers, $\rho_d \chi_m$ (see e.g. Ennis-King & Paterson 2005). The results of Pau *et al.* (2010) confirm this scaling, showing that the time-average of the mass flux is essentially constant after some relatively short onset time, and can be estimated as

$$q_d^m = \alpha \rho_d \chi_m \phi \kappa_d, \tag{3.5}$$

where $\alpha \sim 10^{-2}$ is a dimensionless constant. The volume flux q_d of CO_2 leaving the mobile plume due to convective mixing can then be written

$$q_d = q_d^m / \rho_g = \alpha \chi_v \phi \kappa_d. \tag{3.6}$$

We expect this expression to be valid until the water beneath the plume begins to saturate with dissolved CO_2, at which time the rate of solubility trapping should decrease. For simplicity, we account for this saturating effect by setting the rate of solubility trapping to zero at each position x when the water at that position becomes completely saturated with dissolved CO_2. For this purpose, we track the thickness $h_d(x, t)$ of the 'curtain' of water with dissolved CO_2 that builds beneath the plume (i.e. the blue region in figure 2). We set the rate of solubility trapping to zero when the water beneath the plume is completely saturated, i.e. when $h_1 + h_d = H$. We discuss the curtain in § 3.4.

3.3. *Solubility trapping and capillary trapping*

Solubility trapping enters the mass balance as a loss term $\mathscr{L} < 0$ on the right-hand side of (2.1),

$$(1 - S_{wc})\phi \widetilde{\mathscr{R}} \frac{\partial h_1}{\partial t} + \frac{\partial F_g}{\partial x} = \mathscr{L}, \tag{3.7}$$

where F_g is as defined in (2.2). When $\partial F_g/\partial x = 0$, (3.7) implies that the interface retreats at speed $\mathscr{L}/(1 - S_{wc})\phi \widetilde{\mathscr{R}}$. Equation (2.3) gives $\widetilde{\mathscr{R}} = 1 - \Gamma$ in this scenario
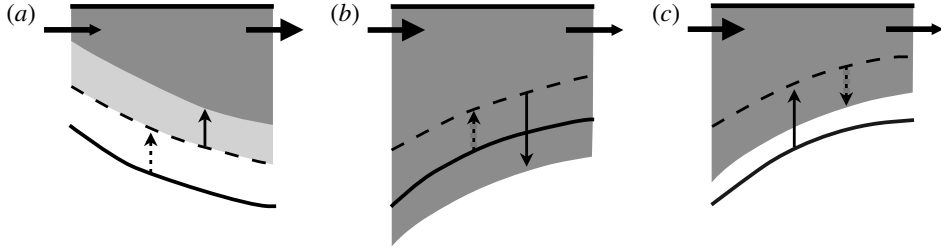
FIGURE 4. We assume that interface displacements due to solubility trapping do not contribute to capillary trapping (§ 3.3). Here, we consider this modelling choice in the context of three possible scenarios for local interface displacement. The local position of the CO_2–water interface is shown before (solid black line) and after (shaded dark grey) displacement due to solubility trapping and flux of mobile CO_2 through the plume. Although these processes occur simultaneously, we suppose for illustration that they occur sequentially. We suppose that solubility trapping occurs first, displacing the interface from its original position (solid black line) to a hypothetical intermediate position (dashed black line), as indicated (vertical dashed black arrow). We then consider the net flux of mobile CO_2 through this portion of the plume. (*a*) When the flux of mobile CO_2 into this portion of the plume (small, horizontal black arrow) is less than the flux of mobile CO_2 out of this portion of the plume (large, horizontal black arrow), the net flux is negative and the interface retreats (vertical black arrow) to its final position (shaded dark grey), while leaving behind residual CO_2 (shaded light grey). Solubility trapping enhances imbibition in this scenario, but we assume that the component of interface motion due to solubility trapping (vertical dashed black arrow) does not cause additional capillary trapping. (*b*) When the net flux is positive and large, the interface experiences net drainage as the interface advances to its final position and no capillary trapping occurs. (*c*) When the net flux is positive and small, the interface may experience net imbibition. However, we assume that no capillary trapping occurs because any residual CO_2 would dissolve as the water imbibes. As a result of this modelling choice, capillary and solubility trapping are effectively decoupled.

since $\partial h/\partial t < 0$, but we argue that capillary trapping should not contribute to the speed of the interface here because residual CO_2 should also dissolve as the interface is displaced upward. We further argue that when $\partial F_g/\partial x > 0$ such that the interface retreats faster than by solubility trapping alone, it is only this flow-driven component of imbibition that contributes to capillary trapping (figure 4). This motivates the definition

$$\mathcal{L} = \begin{cases} -\widetilde{\mathcal{R}}\,(1 - S_{wc})q_d & \text{if } h_d < H - h_1, \\ 0 & \text{otherwise,} \end{cases} \tag{3.8}$$

where the rate of solubility trapping is reduced by $(1 - S_{wc})$ because the presence of the connate water reduces the CO_2–water interfacial area by this amount, and $\mathcal{L} \to 0$ where the water beneath the plume is saturated (§ 3.4). We include $\widetilde{\mathcal{R}}$ in $\mathcal{L}$ so that interface displacements due to solubility trapping do not contribute to capillary trapping. We also modify the definition of $\widetilde{\mathcal{R}}$,

$$\widetilde{\mathcal{R}} = \begin{cases} 1 & \text{if } \partial h_1/\partial t > -q_d/\phi \text{ and } h_2 = 0, \\ 1 - \Gamma & \text{otherwise.} \end{cases} \tag{3.9}$$

Again, this is physically motivated by the expectation that residual CO_2 must also dissolve as the interface is displaced unless the interface moves faster than by

solubility trapping alone (figure 4). These definitions effectively decouple the processes of capillary and solubility trapping.

3.4. *The curtain of water with dissolved* CO_2

We assume that a layer of fully saturated water builds beneath the plume as CO_2 dissolves. We denote the thickness of this 'curtain' of water with dissolved CO_2 by $h_d(x, t)$. We write the conservation law for the thickness of the curtain as

$$\chi_v \phi \frac{\partial h_d}{\partial t} + \chi_v \frac{\partial F_d}{\partial x} = -\frac{\mathscr{L}}{\widetilde{\mathscr{R}}} - \chi_v S_{wc} \phi \frac{\partial h}{\partial t} - \frac{1 - \widetilde{\mathscr{R}}}{\widetilde{\mathscr{R}}} \frac{\partial F_g}{\partial x}, \qquad (3.10)$$

where F_d is the total horizontal flow of groundwater with dissolved CO_2 through the curtain. The curtain gains volume due to convective mixing via the term $-\mathscr{L}/\widetilde{\mathscr{R}}$, where we divide by the conditional coefficient $\widetilde{\mathscr{R}}$ because dissolution of residual CO_2 at the imbibition front also contributes to the curtain (cf. § 3.3). The curtain either gains or loses volume as connate water is left behind by the plume or swept into the plume during imbibition or drainage, respectively, via the term proportional to S_{wc}. We assume that all connate water is supplied from the curtain, and is therefore fully saturated with dissolved CO_2 before entering the plume. This is a very good assumption in most cases, but will lead to an underestimate of the rate of solubility trapping when the amount of connate water swept into the plume at the drainage front exceeds the volume of saturated water available in the curtain. Lastly, residual CO_2 in the wake of the plume takes up a fraction of the available pore space, and the curtain gains macroscopic volume as a result via the term proportional to $\partial F_g/\partial x$. This term vanishes on portions of the interface that are in drainage.

The curtain is a subset of the groundwater region, so the total horizontal flow of water through the curtain is simply a fraction of the total horizontal flow of groundwater, $F_d = (h_d/h_w)F_w$. We neglect the migration of the dense curtain relative to the ambient groundwater because this occurs with characteristic velocity $\kappa_d \ll \kappa$, much slower than the characteristic velocity of CO_2 migration.

Equations (2.1) and (3.10) are coupled through the loss term $\mathscr{L}$, so we must solve them simultaneously. We discuss this in § 5.

We emphasize that this model for solubility trapping features several key simplifications. First, we have assumed that convective mixing ends abruptly when the water becomes saturated, rather than decreasing gradually. This assumption is reasonable if the rate of solubility trapping decreases quickly to zero as the water saturates; we adopt it here for simplicity, and because we believe it captures the essential dissolution-limiting feature of the finite amount of water beneath the plume. Second, we have assumed that the curtain of water with dissolved CO_2 builds beneath the plume as a layer of fully saturated water. Third, we have not accounted for dissolution of the residual CO_2 except immediately at the imbibition front. This is motivated by the fact that residual CO_2 is located primarily in the wake of the plume, so we do not expect it to impact the migration or solubility trapping of the mobile plume. Fourth, we have neglected lateral spreading of the dense, CO_2-rich groundwater relative to the ambient groundwater. This is motivated by the fact that the CO_2 plume spreads and migrates much faster than this water. The importance of these effects has not yet been studied, but our emphasis here is on deriving insight from a simple but physically reasonable model and we do not expect these effects to have an order-one impact on our results.

4. Model for CO₂ migration with solubility trapping

We now incorporate the model for solubility trapping ((3.8) and (3.9)) into the model for CO_2 migration ((2.1) and (3.10)). The complete model for CO_2 migration with solubility trapping consists of two coupled conservation laws, one for the buoyant plume of mobile CO_2 and the other for the curtain of water saturated with dissolved CO_2. We write them in dimensionless form:

$$\widetilde{\mathscr{R}}\frac{\partial \eta}{\partial \tau} + N_f \frac{\partial f}{\partial \xi} + N_s \frac{\partial}{\partial \xi}[(1-f)\eta] - N_g \frac{\partial}{\partial \xi}\left[(1-f)\eta\frac{\partial \eta}{\partial \xi}\right] = -\widetilde{\mathscr{R}}N_d, \qquad (4.1)$$

and

$$\frac{\partial \eta_d}{\partial \tau} + (1-S_{wc})N_f \frac{\partial f_d}{\partial \xi} - (1-S_{wc})N_s \frac{\partial}{\partial \xi}[f_d\eta]$$

$$+ (1-S_{wc})N_g \frac{\partial}{\partial \xi}\left[f_d\eta\frac{\partial \eta}{\partial \xi}\right] = \frac{N_d}{\Gamma_d} - S_{wc}\frac{\partial \eta}{\partial \tau} - (1-\widetilde{\mathscr{R}})\left(\frac{\partial \eta}{\partial \tau} + N_d\right). \qquad (4.2)$$

The primary variables are $\eta = h_1/H$, which is the local thickness of the plume of CO_2 scaled by the thickness of the aquifer, and $\eta_d = h_d/H$, which is the local thickness of the curtain of water saturated with dissolved CO_2, again scaled by the thickness of the aquifer. The nonlinear functions f and f_d are given by

$$f(\eta) = \frac{\mathscr{M}\eta}{\mathscr{M}\eta + (1-\eta)}, \quad f_d(\eta, \eta_d) = \frac{\eta_d}{\mathscr{M}\eta + (1-\eta)}, \qquad (4.3)$$

where $\mathscr{M} = \lambda_1/\lambda_3$ is the mobility ratio. These functions reflect the fact that the aquifer is confined, so that the plume of CO_2 must displace the ambient fluid (groundwater) in order to migrate.

The dimensionless time is $\tau = t/T_c$, where T_c is an appropriate characteristic time. The dimensionless x-coordinate is $\xi = x/L_c$, where L_c is an appropriate characteristic length. We discuss the specific choice of these characteristic values for the injection period in § 4.1, and for the post-injection period in § 4.2.

The model includes capillary and solubility trapping, migration due to groundwater flow and aquifer slope, and buoyant spreading against the caprock. The conditional coefficient $\widetilde{\mathscr{R}}$ captures capillary trapping, changing value depending on whether the interface is locally in drainage or imbibition,

$$\widetilde{\mathscr{R}} = \begin{cases} 1 & \text{if } \partial\eta/\partial\tau > -N_d, \\ 1 - \Gamma & \text{otherwise.} \end{cases} \qquad (4.4)$$

The capillary trapping number Γ measures the amount of residual fluid that is left behind as the interface recedes during imbibition.

Both conservation laws have three flux terms, with coefficients N_f, N_s, and N_g. These terms capture migration due to groundwater flow, migration due to aquifer slope, and buoyant spreading due to gravity, respectively. The coefficients are given by

$$N_f = \frac{T_c}{T_i}\frac{Q}{Q_i/2}, \quad N_s = \frac{T_c}{L_c}\kappa \sin\vartheta, \quad N_g = \frac{T_c}{L_c}\kappa \cos\vartheta \frac{H}{L_c}, \qquad (4.5)$$

where L_c is the characteristic length (4.7), T_c is the characteristic time (§§ 4.1 and 4.2), and Q is the net volume flow of fluid through the aquifer from left to right (§§ 4.1 and 4.2); κ is the characteristic buoyancy-driven velocity of the plume (2.5).

The sink term with coefficient N_d on the right-hand side of (4.1) captures the loss of CO$_2$ from the plume due to solubility trapping via convective dissolution. N_d is given by

$$N_d = \begin{cases} \alpha \chi_v \kappa_d \dfrac{T_c}{H} & \text{if } \eta(\xi, \tau) > 0 \text{ and } \eta_d(\xi, \tau) < (1 - \eta(\xi, \tau)), \\ 0 & \text{otherwise,} \end{cases} \tag{4.6}$$

taking a constant value until the water beneath the plume becomes saturated with dissolved CO$_2$, and changing to zero locally as the water saturates. We assume that the water beneath the plume is locally saturated with dissolved CO$_2$ when the curtain of water saturated with dissolved CO$_2$ reaches the bottom of the aquifer ($\eta + \eta_d = 1$).

The curtain grows as CO$_2$ dissolves from the plume. Each unit volume of CO$_2$ that dissolves from the plume becomes $1/\Gamma_d$ units of volume in the curtain, where the constant $\Gamma_d = \chi_v/(1 - S_{wc})$. The curtain also gains and loses volume due to the transfer of residual CO$_2$ and connate (residual) water across the CO$_2$–water interface as the plume migrates (§ 3.4); the source/sink terms on the right-hand side of (4.2) account for these effects.

Without loss of generality, we choose $N_f \geqslant 0$ so that groundwater flow is always to the right by convention. Aquifer slope can be either positive ($N_s > 0$) for anticlockwise aquifer tilt or negative ($N_s < 0$) for clockwise aquifer tilt.

4.1. *The injection period*

During injection, we assume that a constant volume flow rate Q_i of CO$_2$ per unit length of the line-drive well array is pumped into the aquifer. We take the characteristic time scale to be the duration of injection, $T_c = T_i$, so that $\tau = 1$ is the end of the injection period.

As in Part 1, we choose the characteristic length scale during injection to be the length of a rectangle of aquifer of height H and containing a volume equal to one-half of the total volume of CO$_2$ to be injected, $Q_i T_i/2$:

$$L_c = Q_i T_i / 2(1 - S_{wc})\phi H. \tag{4.7}$$

Injection typically dominates the flow, so we neglect natural groundwater flow and slope relative to injection and assume that the flow rate Q_i is split evenly between the left and right sides of the injection well. We then have that $Q = U_n H + Q_i/2 \approx Q_i/2$, so that

$$N_f^i = 1, \quad N_s^i = \frac{\Delta\rho g k \lambda_g H}{Q_i/2} \sin\vartheta, \quad N_g^i = \frac{\Delta\rho g k \lambda_g (1 - S_{wc})\phi H^3}{(Q_i/2)^2 T_i} \cos\vartheta, \tag{4.8}$$

and

$$N_d^i = \begin{cases} \alpha \chi_v \kappa_d \dfrac{T_i}{H} & \text{if } \eta(\xi, \tau) > 0 \text{ and } \eta_d(\xi, \tau) < (1 - \eta(\xi, \tau)), \\ 0 & \text{otherwise.} \end{cases} \tag{4.9}$$

The superscript i indicates that these are the values of these parameters during injection. Typically $N_s^i, N_g^i \ll 1$, so the plume shape will be symmetric across the injection well. We discuss the impact of solubility trapping during injection in § 5.1.

4.2. *Post-injection migration*

Once injection has stopped, the net flow of fluid through the aquifer, Q, is due only to natural groundwater flow. We therefore have that $Q = U_n H$ in the post-injection period.

The characteristic length scale from the injection period was based on the total amount of CO_2 injected (4.7). This is also an appropriate choice for the post-injection period because it is characteristic of the initial length of the now-migrating plume, so we retain it.

The characteristic time scale from the injection period was the injection time. This is not an appropriate choice for the post-injection period because CO_2 migration due to slope and/or groundwater flow is typically very slow relative to injection. In order to choose a new characteristic time while keeping $\tau = 1$ as the end of injection, we redefine the dimensionless time in post-injection as

$$\tau = 1 + \frac{t - T_i}{T_c}, \tag{4.10}$$

so that the end of injection, $t = T_i$, corresponds to $\tau = 1$ for any choice of characteristic time T_c. A characteristic time for post-injection can be derived from any one of the four rates associated with post-injection migration and trapping: the rate of migration due to groundwater flow, the rate of migration due to aquifer slope, the rate of buoyant spreading against the caprock, or the rate of solubility trapping due to convective mixing. For a specific aquifer, the choice should be guided by the dominant mechanism. When no one mechanism is dominant, which is often the case in continental sedimentary basins (Garven 1995), the specific choice is arbitrary.

Here, we choose a characteristic time based on the rate of migration due to groundwater flow:

$$T_c = \frac{Q_i T_i / 2}{U_n H}. \tag{4.11}$$

For this choice, we have that ((4.5) and (4.6) with $Q = U_n H$ and $T_c = Q_i T_i / 2 U_n H$)

$$N_f = 1, \quad N_s = \frac{\Delta \rho g k \lambda_g}{U_n} \sin \vartheta, \quad N_g = \frac{\Delta \rho g k \lambda_g (1 - S_{wc}) \phi H^2}{U_n (Q_i / 2) T_i} \cos \vartheta \tag{4.12}$$

and

$$N_d = \begin{cases} \alpha \chi_v \kappa_d \dfrac{Q_i T_i / 2}{U_n H^2} & \text{if } \eta(\xi, \tau) > 0 \text{ and } \eta_d(\xi, \tau) < (1 - \eta(\xi, \tau)), \\ 0 & \text{otherwise.} \end{cases} \tag{4.13}$$

Here, N_s gives the importance of advection due to slope relative to that due to groundwater flow; N_g gives the importance of diffusive spreading due to buoyancy relative to advection due to groundwater flow, analogous to the inverse of a Péclet number in mass transfer; and N_d gives the importance of loss due to solubility trapping relative to advection due to groundwater flow, analogous to a Damköhler number in reactive transport.

A consequence of this choice of characteristic time is that $N_f \equiv 1$. We retain N_f in the analysis (§ 5) and report our results (§ 6) in terms of the ratios N_s/N_f, N_g/N_f, and N_d/N_f so that the results remain relevant for other choices of the characteristic time.

The choice of a characteristic time based on groundwater flow will not be appropriate when groundwater flow is 'weak' compared to slope, buoyancy, or solubility trapping. In these cases, a different characteristic time should be used in (4.5) and (4.6) to derive the appropriate expressions for N_f, N_s, N_g, and N_d.

5. CO$_2$ migration with capillary and solubility trapping

We now study injection and post-injection migration with capillary and solubility trapping. We note that the macroscopic features of CO$_2$ migration and trapping – in particular, the prominent gravity tongue, the position of the leading edge, and the shape of the profile of residual gas – are little affected by even large values of N_g compared to N_f or N_s (Juanes & MacMinn 2008; Hesse *et al.* 2008). We therefore neglect the buoyant spreading term to simplify the analysis, as in Part 1 (see figure 3 of Part 1). In this limit, (4.1) and (4.2) are of hyperbolic character.

After neglecting the spreading term, it will be useful to rewrite (4.1) in terms of a scaled and shifted dimensionless plume thickness g, as in Part 1,

$$\frac{\partial g}{\partial \tau} + \frac{1}{\widetilde{\widetilde{\mathscr{R}}}} \frac{\partial}{\partial \xi} G(g) = -(\mathscr{M} - 1)N_d, \tag{5.1}$$

where $g = (\mathscr{M} - 1)\eta + 1$ remaps $0 \leqslant \eta \leqslant 1$ to $1 \leqslant g \leqslant \mathscr{M}$, and G is the corresponding flux function,

$$G(g) = \mathscr{M} N_f \left[1 - \frac{1}{g} \right] + \frac{N_s}{\mathscr{M} - 1} \left[(\mathscr{M} + 1) - g - \frac{\mathscr{M}}{g} \right]. \tag{5.2}$$

Equation (5.1) is a first-order, nonlinear, autonomous, hyperbolic conservation law with a sink term. The solution to this equation depends on seven dimensionless parameters: $\mathscr{M}$, Γ, Γ_d, S_{wc}, N_f, N_s, and N_d. One of the latter three parameters can always be subsumed into the characteristic time scale, so the solution depends uniquely only on the ratios of any two of them to the third. For generality, we retain all three parameters in the analysis that follows; however, we present the results (§ 6) in terms of the ratios N_s/N_f and N_d/N_f because we choose a characteristic time scale based on groundwater flow (§ 4.2).

Note that the values of $\mathscr{M}$ and Γ used in the figures throughout this section (figures 5–9) are chosen for illustration only, to make the noteworthy features of the plume shapes and characteristics clearly visible. In practice, these values of $\mathscr{M} = 2$ and $\Gamma = 0.5$ are too low and too high, respectively. We use realistic values of $\mathscr{M} = 5$–15 and $\Gamma = 0.3$ when presenting the key results in § 6 (figures 10–13).

5.1. *The injection period*

We derive here the shape of the plume at the end of the injection period, because this serves as the initial condition for post-injection migration (Juanes & MacMinn 2008; MacMinn & Juanes 2009; Juanes *et al.* 2010).

As discussed in § 4.1, we assume that injection dominates the flow during the injection period, and we therefore take $N_f^i = 1$ and $N_s^i, N_g^i \ll 1$. As a result, the injected CO$_2$ is split evenly between the left and right sides of the injection well and the plume shape is symmetric across the injection well.

To assess the impact of solubility trapping on the plume shape during injection, we compare the rate of CO$_2$ injection, Q_i, to an estimate of the rate of solubility trapping, Q_d. The upscaled rate of solubility trapping per unit length of CO$_2$–water interface is $(1 - S_{wc})q_d$ (§ 3.2). Without solubility trapping, the extent of the plume at the end of injection is $2\mathscr{M} Q_i T_i/(1 - S_{wc})\phi H$ (§ 2.2 of Part 1). We then estimate

$$\frac{Q_d}{Q_i} \sim \frac{q_d \mathscr{M} Q_i T_i}{\phi H Q_i} = \mathscr{M} N_d^i. \tag{5.3}$$
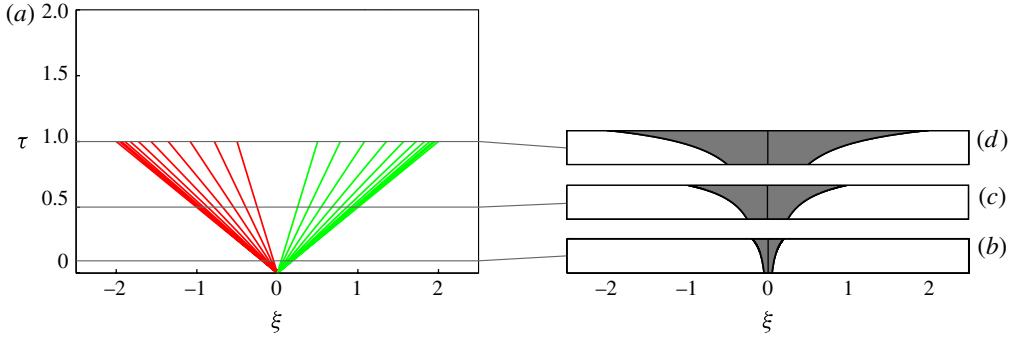
FIGURE 5. (Colour online) During injection with $\mathcal{M} = 2$, (*a*) the evolution of the plume in characteristic space and (*b*)–(*d*) the shape of the plume (grey) at $\tau = 0.1$, 0.5, and 1, respectively. In (*a*), we show several waves of the left and right fronts in dark grey (red online) and light grey (green online), respectively; the innermost and outermost waves on each front correspond to $g = \mathcal{M}$ and $g = 1$ ($\eta = 1$ and $\eta = 0$), respectively.

Taking typical but conservative values, $\mu_w = 5.5 \times 10^{-4}$ Pa s, $\mu_g = 6 \times 10^{-5}$ Pa s, $\chi_v = 0.1$, $S_{wc} = 0.4$, $\phi = 0.15$, $\Delta\rho_d = 10$ kg m^{-3}, $k = 100$ mD $= 10^{-13}$ m^2, $T_c = T_i = 30$ years, $H = 100$ m, we find that $Q_d/Q_i \sim 10^{-2}$, implying that the fraction of the CO_2 that dissolves during injection is negligible. Note that we have neglected the onset time for convective mixing as well as the finite supply of water, both of which would decrease the amount of CO_2 that would dissolve during injection. We have also used the extent of the plume at the end of injection, again giving an overestimate of the amount of CO_2 that would dissolve during injection. We therefore conclude that solubility trapping is negligible during injection and we use the injection solution of Nordbotten & Celia (2006) and Verdon & Woods (2007), as in Part 1. Modelling the well as a line source located at $\xi = 0$ with strength $Q_i/2H$ per unit length, the solution from the method of characteristics is

$$\xi_L^i(g, \tau) = -\left(\frac{\mathcal{M}}{g^2}\right)\tau, \quad \xi_R^i(g, \tau) = \left(\frac{\mathcal{M}}{g^2}\right)\tau, \tag{5.4}$$

where the left front, ξ_L^i, is the reflection of the right front, ξ_R^i. Figure 5 shows the characteristics and the plume shape at several times during the injection period, which ends at $\tau = 1$.

5.2. *Post-injection migration*

Once injection has ended, the plume migrates due to slope and groundwater flow, and shrinks due to capillary and solubility trapping. The migration behaviour is given by the solution to (4.1) and (4.2), which are nonlinear conservation laws coupled by mass transfer due to convective mixing. These must be solved numerically in general, but we are able to derive semi-analytical solutions in two limiting cases: when the water beneath the plume saturates very slowly or very quickly relative to plume migration (figure 6). When the water beneath the plume saturates with dissolved CO_2 slowly relative to plume migration, the curtain does not interact with the bottom of the aquifer. In this slow-saturation limit, (5.1) can be solved independently of (4.2). When the water beneath the plume saturates with dissolved CO_2 very quickly relative to plume migration, the water beneath the plume will be completely saturated except
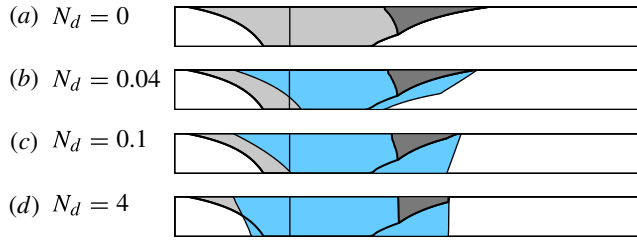
FIGURE 6. (Colour online) The rate at which the water beneath the plume saturates with dissolved CO$_2$ depends on the speed of migration, the length of the plume, the rate of solubility trapping, and the amount of dissolved CO$_2$ the water can hold. Here we show the shape of the plume (dark grey) and the curtain (mid grey (blue online)) at $\tau = 2.5$ from numerical solutions to (4.1) and (4.2) for fixed $\mathcal{M} = 2$, $\Gamma = 0.5$, $\Gamma_d = 0.1$, $N_f = 1$, $N_s = -0.75$, $N_g = 0$, and for N_d increasing from 0 to 4, as indicated. Where the curtain reaches the bottom of the aquifer, convective mixing has stopped because the water is saturated. We identify two limits: (*b*) when the water saturates slowly relative to plume migration, solubility trapping is not limited by the amount of water beneath the plume, and (*d*) when the water saturates very quickly (instantaneously) relative to plume migration, the water beneath the plume is completely saturated with dissolved CO$_2$ and only the leading edge of the plume dissolves as it migrates.

at the leading edge. In this instantaneous-saturation limit, the majority of the plume will not experience solubility trapping as it migrates and (5.1) can again be solved independently of (4.2). Below, we develop semi-analytical solutions to (5.1) in these two limits.

5.3. *The slow-saturation limit*

When the water beneath the plume saturates with dissolved CO$_2$ slowly compared to plume motion, solubility trapping from the plume is not limited by the supply of water and (5.1) can be solved independently of (4.2). In this limit, we develop semi-analytical solutions to (5.1) via the method of characteristics. Note that CO$_2$ migration becomes independent of Γ_d in this limit because the water does not saturate. All of the expressions and results for this limit simplify to those from Part 1 when $N_d = 0$.

5.3.1. *Post-injection migration in the slow-saturation limit*

We begin with (5.1), moving the loss term inside the time derivative,

$$\frac{\partial}{\partial \tau}[g + (\mathcal{M} - 1)N_d(\tau - 1)] + \frac{1}{\widetilde{\mathcal{R}}}\frac{\partial}{\partial \xi}G(g) = 0. \qquad (5.5)$$

We then introduce a new variable g_0 such that $g = g_0 - (\mathcal{M} - 1)N_d(\tau - 1)$, and we write

$$\frac{\partial g_0}{\partial \tau} + \frac{1}{\widetilde{\mathcal{R}}}\frac{\partial}{\partial \xi}[G(g_0 - (\mathcal{M} - 1)N_d(\tau - 1))] = 0. \qquad (5.6)$$

Equation (5.6) is a nonlinear hyperbolic conservation law in g_0; note that it is not autonomous because τ appears explicitly in the flux function G. The solution is a collection of waves travelling through space–time. Physically, g_0 is the thickness of each wave at the end of injection ($g = g_0$ at $\tau = 1$) and this initial thickness is constant in time for each wave. The current thickness of each wave is $g = g_0 - (\mathcal{M} - 1)N_d(\tau - 1)$,

which shrinks in time at a constant rate due to solubility trapping. Waves travel with speed $G'/\widetilde{\mathscr{R}}$, where

$$G' = \frac{\partial G}{\partial g_0} = -\left[\frac{1}{\mathscr{M} - 1}N_s\right] + \left[\mathscr{M}N_f + \frac{\mathscr{M}}{\mathscr{M} - 1}N_s\right]\frac{1}{g^2}. \tag{5.7}$$

Note that the velocity at which each wave propagates is a function of its current thickness, and that this function $G'(g)$ is the same as in Part 1. Unlike in Part 1, waves no longer travel at constant velocity because all waves now shrink in time due to solubility trapping.

As in Part 1, the post-injection problem is more difficult than the injection problem because of the complex interactions between slope, groundwater flow, capillary trapping, and now solubility trapping – waves collide, and we divide the analysis into parts based on the types of collisions that occur. The derivative of the flux function again changes sign once at the stationary point $g = g_s$ given by

$$g_s = \sqrt{\mathscr{M}(\mathscr{M} - 1)N_f/N_s + \mathscr{M}}, \tag{5.8}$$

and we can again divide the range of possible values of the ratio N_s/N_f into three intervals based on the nature of the resulting plume migration, and these intervals are the same as in Part 1 since G' is unchanged. For $N_s/N_f \leqslant -\mathscr{M}$, the negative-slope-with-weak-flow interval, the flux function is concave up and has a local minimum, so that G' vanishes at $g = g_s$ and is negative for $g < g_s$ and positive for $g > g_s$. For $-\mathscr{M} < N_s/N_f < 1$, the flow-with-weak-slope interval, the flux function is concave up for $N_s/N_f < -(\mathscr{M} - 1)$, linear for $N_s/N_f = -(\mathscr{M} - 1)$, and concave down for $N_s/N_f > -(\mathscr{M} - 1)$, and in all cases strictly increasing so that G' is positive. For $1 \leqslant N_s/N_f$, the positive-slope-with-weak-flow interval, the flux function is concave down and has a local maximum, so that G' vanishes at $g = g_s$ and is positive for $g < g_s$ and negative for $g > g_s$. Note that, unlike in Part 1, any single wave is only instantaneously stationary as its current thickness passes through the value g_s, which occurs at time

$$\tau_s = 1 + \frac{g_0 - g_s}{(\mathscr{M} - 1)N_d}. \tag{5.9}$$

For simplicity, we restrict our analysis here to the flow-with-weak-slope interval, $-\mathscr{M} < N_s/N_f < 1$, for which G' is strictly positive. Outside that interval, a stationary point exists on the plume and both fronts have a portion that is in drainage and a portion that is in imbibition. This complicates the solution because waves may change direction as they shrink. That is, drainage waves may at some point become imbibition waves and vice-versa. While the procedure presented below is general and could be used to develop semi-analytical solutions outside the flow-with-weak-slope interval, the complexity of doing so is prohibitive in practice.

It is straightforward to rewrite the definition of the conditional accumulation coefficient $\widetilde{\mathscr{R}}$ in terms of g_0,

$$\widetilde{\mathscr{R}} = \begin{cases} 1 & \text{if } \partial g_0/\partial \tau > 0, \\ 1 - \Gamma & \text{otherwise,} \end{cases} \tag{5.10}$$

The direction in which each wave travels (i.e. to the left, or to the right) is again determined by the sign of $G'(g)$, and this in turn sets the appropriate value of $\widetilde{\mathscr{R}}$ for each wave. Waves of the left front moving to the left correspond to CO_2 displacing

groundwater, and are then drainage waves; waves of the left front moving to the right correspond to groundwater displacing CO$_2$, and are imbibition waves. Waves of the right front moving to the left or to the right are similarly imbibition waves or drainage waves, respectively. Note that all waves shrink vertically in time due to solubility trapping, but this component of imbibition does not contribute to capillary trapping by construction of the model (§ 3.3).

Now starting from the end-of-injection shape, all waves propagate to the right at speed $G'(g)/\widetilde{R}$ until two or more waves collide. The right front is a drainage front with $\widetilde{\mathscr{R}} = 1$, and the left front is an imbibition front with $\widetilde{\mathscr{R}} = (1 - \varGamma)$. Because of this, a given wave on the left front travels faster than the corresponding wave on the right front.

Given the position of each wave at $\tau = 1$ and its instantaneous velocity in post-injection, we can write the position of each wave on the left and right fronts by integrating the velocity in time,

$$\xi_L = -\frac{\mathscr{M}}{g_0^2} + \frac{1}{1 - \varGamma} \left(-\left[\frac{N_s}{\mathscr{M} - 1} \right] + \left[\mathscr{M} N_f + \frac{\mathscr{M}}{\mathscr{M} - 1} N_s \right] \frac{1}{gg_0} \right) (\tau - 1),$$
$$(5.11a)$$

$$\xi_R = \frac{\mathscr{M}}{g_0^2} + \left(-\left[\frac{N_s}{\mathscr{M} - 1} \right] + \left[\mathscr{M} N_f + \frac{\mathscr{M}}{\mathscr{M} - 1} N_s \right] \frac{1}{gg_0} \right) (\tau - 1), \quad (5.11b)$$

where, again, g_0 is the initial thickness of each wave and $g = g_0 - (\mathscr{M} - 1)N_d(\tau - 1)$ is the current thickness of each wave. These expressions are valid for all waves with current thickness $g > 1$ ($\eta > 0$), and that have not yet collided with other waves.

When the current thickness of a wave decreases below $g = 1$, that wave has dissolved completely and ceases to exist. The left and right edges of the plume are then formed by the leftmost and rightmost waves that still exist at time τ. As in Part 1, we refer to the position of the leftmost wave on left front and of the rightmost wave on the right front as ξ_{LL} and ξ_{RR}, respectively. These positions correspond to the waves with current thickness $g = 1$ and therefore with original thickness $g_0 = 1 + (\mathscr{M} - 1)N_d(\tau - 1)$. These waves do not correspond to characteristics because the characteristics here are waves with constant original thickness and shrinking current thickness. The expressions for ξ_{LL} and ξ_{RR} are readily evaluated from (5.11) for these values of g and g_0.

Depending on the shape of the flux function, waves will either accelerate or decelerate as they shrink. When the flux function is concave down ($N_s/N_f > -(\mathscr{M} - 1)$), wave velocity increases monotonically with wave thickness and waves accelerate as they shrink. Because of this acceleration, the entire left front does not compact into a shock simultaneously. Rather, an incipient shock forms at the leftmost point on the left front, ξ_{LL}, and builds from left to right as waves accelerate, until the entire left front is part of the shock. We find the time τ_{LL}^σ at which this incipient shock would form by solving for the time at which $\partial \xi_L / \partial g$ vanishes at the leftmost point. This gives the time of shock formation implicitly,

$$(\mathscr{M} - 1)^2 N_d^2 (\tau_{LL}^\sigma - 1)^3 + 3(\mathscr{M} - 1)N_d (\tau_{LL}^\sigma - 1)^2$$
$$+ 2(\tau_{LL}^\sigma - 1) = 2\frac{(1 - \varGamma)(\mathscr{M} - 1)}{(\mathscr{M} - 1)N_f + N_s}. \quad (5.12)$$

With $N_d = 0$, this expression simplifies readily to the time at which the entire left front would compact into a shock in the absence of solubility trapping (τ_{LL}^{LR}, equation (3.5a) from Part 1).

Similarly, wave velocity decreases monotonically with wave thickness when the flux function is concave up ($N_s/N_f < -(\mathcal{M} - 1)$), and waves decelerate as they shrink. Here, shock formation begins with an incipient shock at the rightmost point on the right front, ξ_{RR}, and builds from right to left as waves decelerate, until the entire right front is part of the shock. We find the time τ_σ^{RR} at which this incipient shock would form by solving for the time at which $\partial \xi_R/\partial g$ vanishes at the rightmost point. This gives the time of shock formation implicitly,

$$(\mathcal{M} - 1)^2 N_d^2 (\tau_\sigma^{RR} - 1)^3 + 3(\mathcal{M} - 1)N_d (\tau_\sigma^{RR} - 1)^2$$
$$+ 2(\tau_\sigma^{RR} - 1) = -2\frac{(\mathcal{M} - 1)}{(\mathcal{M} - 1)N_f + N_s}. \tag{5.13}$$

With $N_d = 0$, this expression simplifies readily to the time at which the entire right front would compact into a shock in the absence of solubility trapping (equation (3.5c) from Part 1).

In the particular case when the flux function is a straight line ($N_s/N_f = -(\mathcal{M} - 1)$), wave speed is independent of wave thickness. The fronts will not change shape as they migrate and dissolve, and no shock will form. Accordingly, (5.12) and (5.13) degenerate for this value of N_s/N_f, and have no solution.

The migration behaviour may also change if the rightmost point on the left front, ξ_{LR}, collides with the leftmost point on the right front, ξ_{RL}, forming a peak. Unlike ξ_{LL} and ξ_{RR}, these positions correspond to characteristics: they are the waves with original thickness $g_0 = \mathcal{M}$ and current thickness $g = \mathcal{M} - (\mathcal{M} - 1)N_d(\tau - 1)$. Expressions for ξ_{LR} and ξ_{RL} can be evaluated from (5.11). The time τ_{LR}^{RL} at which these two waves would collide to form a peak is given implicitly by the expression

$$N_s N_d (\tau_{LR}^{RL} - 1)^2 + \left[\frac{2(1 - \Gamma)(\mathcal{M} - 1)N_d}{\mathcal{M}\Gamma} + (N_f - N_s)\right](\tau_{LR}^{RL} - 1)$$
$$= \frac{2(1 - \Gamma)}{\Gamma}. \tag{5.14}$$

With $N_d = 0$, this expression simplifies to the time at which this collision would occur in the absence of solubility trapping (equation (3.5b) from Part 1).

What remains is to divide the flow-with-weak-slope interval into cases based on the order in which these collisions occur. We did so explicitly in Part 1, finding five cases within this interval. The five possible cases here are the same as in Part 1, and are as follows: in case 1, an incipient shock forms on the left and consumes the entire left front before a peak forms; in case 2, an incipient shock forms on the left and a peak forms at the bottom of the plume, and then the shock collides with the peak; in case 3, a peak forms at the bottom of the plume and no shock forms; in case 4, an incipient shock forms on the right and a peak forms at the bottom of the plume, and then the peak collides with the shock; and in case 5, an incipient shock forms on the right and consumes the entire right front before a peak forms. The delineation between these cases now depends on N_d in addition to $\mathcal{M}$, Γ, and N_s/N_f, and we are no longer able to delineate them explicitly because the collision times (in particular, τ_{LL}^σ and τ_σ^{RR}) are defined implicitly. Instead, we implement a decision-tree algorithm to evaluate and compare these times, and evolve the plume accordingly. We describe in detail the remainder of the development for case 2.

5.3.2. *Flow with weak slope, case 2, in the slow-saturation limit*

In case 2, the first two collisions are the development of an incipient shock at the left, which occurs at time τ_{LL}^σ, and the formation of a peak at the bottom, which occurs at time τ_{LR}^{RL}. The ordering of these two collisions is unimportant. The peak is formed by the intersection of the left and right fronts, and the initial thickness $g_{0,p}$ of the waves forming the peak at time τ is given implicitly by

$$
\left[\frac{N_s}{\mathcal{M}-1}(\tau-1)\right]g_{0,p}^3 + \left[\frac{2\mathcal{M}(1-\Gamma)}{\Gamma} - \left(\mathcal{M}N_f + \frac{\mathcal{M}}{\mathcal{M}-1}N_s\right)(\tau-1)\right]g_{0,p}
$$
$$
+ [N_s N_d(\tau-1)^2]g_{0,p}^2 - \left[\frac{2\mathcal{M}(1-\Gamma)}{\Gamma}(\mathcal{M}-1)N_d(\tau-1)\right] = 0. \tag{5.15}
$$

The shock, once it has formed, collides continuously with waves of the left front as it grows. To construct the differential equation describing the growth of the shock, we begin by posing the collision of the shock at time $\tau^\star$ with an arbitrary wave of the left front of initial thickness $g_0^\star$ and current thickness $g^\star$. The position of the shock at time $\tau^\star$ can be written

$$
\xi_\sigma^\star = \xi_\sigma(\tau^\star) = \xi_{LL}^\sigma + \int_{\tau_{LL}^\sigma}^{\tau^\star} \sigma \, d\tau. \tag{5.16}
$$

The shock speed σ is evaluated from the Rankine–Hugoniot condition (see e.g. Lax 1972),

$$
\sigma(g^\star) = \frac{1}{1-\Gamma}\frac{[\![G]\!]}{[\![g]\!]} = \frac{1}{1-\Gamma}\frac{G(g^\star)}{g^\star - 1}, \tag{5.17}
$$

where the notation $[\![\circ]\!]$ indicates the difference or 'jump' in the indicated quantity across the shock. Note that only the current thicknesses of the waves on either side of the shock influence the instantaneous shock speed. The position at time $\tau^\star$ of the wave with initial thickness $g_0^\star$ is

$$
\xi^\star = \xi(g^\star, \tau^\star) = -\frac{\mathcal{M}}{g_0^{\star 2}} + \frac{1}{1-\Gamma}\int_1^{\tau^\star} G'(g^\star) \, d\tau. \tag{5.18}
$$

Equating $\xi_\sigma^\star$ with $\xi^\star$, since these must be equal by the definition of $g^\star$ and $\tau^\star$, we differentiate the resulting expression with respect to $\tau^\star$ and rearrange to find an ordinary differential equation (ODE) for the shock height as a function of time,

$$
\frac{dg^\star}{d\tau^\star} = \frac{\sigma(g^\star) - \partial\xi^\star/\partial\tau^\star}{\partial\xi^\star/\partial g^\star}. \tag{5.19}
$$

This ODE is not separable unless $N_d = 0$, so we integrate it numerically from time $\tau^\star = \tau_{LL}^\sigma$ until it collides with the peak, at which time $g^\star(\tau^\star) = g_p(\tau^\star)$. The shock then collides continuously with the right front until the plume vanishes. The development of the ODE for the shock height as a function of time during this period is analogous to that above. We plot the characteristics and plume shapes for case 2 in the slow-saturation limit in figure 7.

5.4. *The instantaneous-saturation limit*

When the water beneath the plume saturates with dissolved CO_2 very quickly relative to plume migration, the majority of the plume migrates over saturated water and is therefore not influenced by solubility trapping. Only the leading edge of the plume
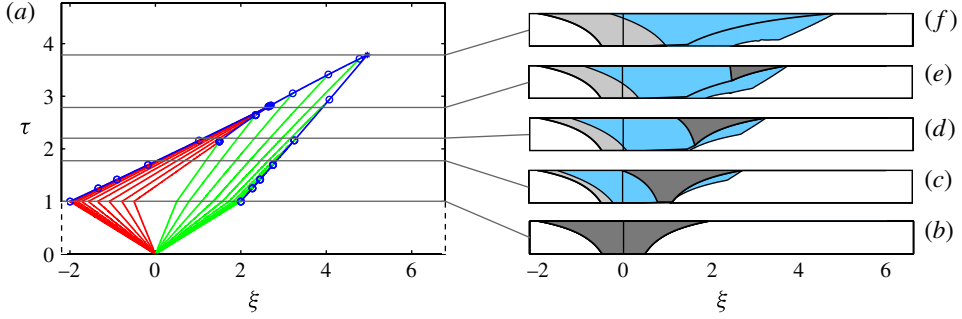
FIGURE 7. (Colour online) Post-injection migration in the slow-saturation limit for case 2 of the flow-with-weak-slope interval, with $\mathcal{M} = 2$, $\Gamma = 0.5$, $N_f = 1$, $N_s = -0.75$, and $N_d = 0.04$. (*a*) The evolution of the plume in characteristic space with waves of the left and right fronts in dark grey (red online) and light grey (green online), respectively, and the paths of the peak, the shock, and the leading and trailing edges of the plume in solid black lines with open circles (blue online). (*b*)–(*f*) The shape of the plume at several times during migration, with mobile CO_2 in dark grey, the region containing residual CO_2 in light grey, the curtain of groundwater with dissolved CO_2 in mid grey (blue online), and groundwater in white. The curtain is approximate (drawn for $\Gamma_d = 0.1$) because we do not solve (4.2) in this limit. The characteristics are not straight lines here because the waves shrink and therefore change speed as they migrate, and also that the leading and trailing edges of the plume are not characteristics, but rather cut across characteristics. For comparison, the characteristics and the plume shapes here are drawn on the same scale in space and time as those in figure 12 in Part 1 and those in figure 9 below. We include the injection period here, but denote that portion of the time axis ($\tau < 1$) with dashed lines to emphasize that the characteristic time scale may change dramatically from injection to post-injection, across $\tau = 1$ (§§ 4.1 and 4.2).

encounters unsaturated water as it migrates, and all of this water must saturate instantaneously as the leading edge travels over it. In this limit, we can again develop semi-analytical solutions to (5.1) via the method of characteristics. Note that CO_2 migration becomes independent of N_d in this limit because the water is assumed to saturate instantaneously. All of the expressions and results for this limit simplify to those from Part 1 when $\Gamma_d = 0$. Although the procedure we use here is general, we again restrict our analysis to the flow-with-weak-slope interval, $-\mathcal{M} < N_s/N_f < 1$, for simplicity.

5.4.1. *Initial condition in the instantaneous-saturation limit*

Because the water beneath the plume saturates instantaneously relative to plume migration, the initial condition for post-injection migration changes instantly from the end-of-injection plume shape to a modified shape as CO_2 from the plume dissolves to saturate the water beneath. Recall from § 5.1 that the end-of-injection shape is assumed to be symmetric across $\xi = 0$. Rearranging (5.4), the right half of the end-of-injection shape is given by

$$\eta_i = \begin{cases} 1 & 0 < \xi < 1/\mathcal{M}, \\ (\sqrt{\mathcal{M}/\xi} - 1)/(\mathcal{M} - 1) & 1/\mathcal{M} < \xi < \mathcal{M}, \\ 0 & \mathcal{M} < \xi. \end{cases} \quad (5.20)$$

The dimensionless volume of the end-of-injection shape is 2. The volume of free-phase CO_2 within an infinitesimal section of the end-of-injection plume at some position ξ is $(1 - S_{wc})\phi\eta_i(\xi)\,d\xi$. The volume of CO_2 that can be dissolved in the water
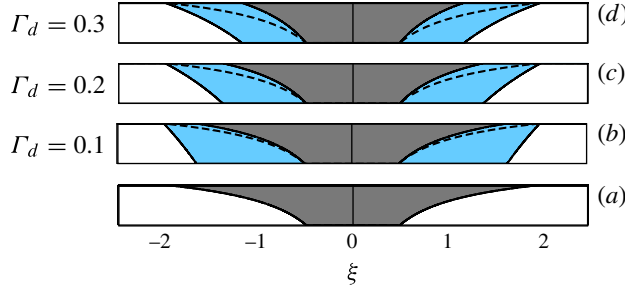
FIGURE 8. (Colour online) In the instantaneous-saturation limit, the plume contracts at $\tau = 1^+$ as the water beneath the end-of-injection plume shape saturates instantaneously with dissolved CO$_2$. We therefore use a modified initial shape for post-injection migration in this limit, as illustrated here for $\mathcal{M} = 2$ (a) at the end of injection (5.20) and (b)–(d) after saturating the water for $\Gamma_d = 0.1$–0.3, as indicated in (5.24). Free-phase CO$_2$ is shown in dark grey, water is shown in white, the curtain of water saturated with dissolved CO$_2$ is shown in mid grey (blue online), and the end-of-injection shape from (a) is indicated in (b)–(d) as a dashed black line.

at the same position ξ is $\phi\chi_v(1 - \eta_0(\xi))\,\mathrm{d}\xi$, where η_0 is the shape of the plume after saturating the water. Conserving the total mass of CO$_2$ at position ξ before and after the water saturates with dissolved CO$_2$, we have that

$$(1 - S_{wc})\phi\eta_i = (1 - S_{wc})\phi\eta_0 + \phi\chi_v(1 - \eta_0), \tag{5.21}$$

which can be rearranged to give

$$\eta_0 = \frac{\eta_i - \Gamma_d}{1 - \Gamma_d}. \tag{5.22}$$

The new initial thickness η_0 goes to 0 at $\eta_i = \Gamma_d$, which occurs at position

$$\xi^\star = \frac{\mathcal{M}}{((\mathcal{M} - 1)\Gamma_d + 1)^2}. \tag{5.23}$$

This is the position where the water column can dissolve exactly as much free-phase CO$_2$ as was present. For $\xi < \xi^\star$, the water saturates completely before dissolving all of the free-phase CO$_2$; for $\xi > \xi^\star$, the free-phase CO$_2$ dissolves completely but is not sufficient to saturate the water. We then have

$$\eta_0 = \begin{cases} 1 & 0 < \xi < 1/\mathcal{M}, \\ (\eta_i - \Gamma_d)/(1 - \Gamma_d) & 1/\mathcal{M} < \xi < \xi^\star, \\ 0 & \xi^\star < \xi. \end{cases} \tag{5.24}$$

We plot (5.24) in figure 8 for several values of Γ_d. The dimensionless volume of this new initial shape is $2/((\mathcal{M} - 1)\Gamma_d + 1)$, where a dimensionless volume $2(\mathcal{M} - 1)\Gamma_d/((\mathcal{M} - 1)\Gamma_d + 1)$ of free-phase CO$_2$ has dissolved. Rewriting (5.24) in terms of characteristics, we have

$$\xi_L^0(g) = -\frac{\mathcal{M}}{((1 - \Gamma_d)g + \mathcal{M}\Gamma_d)^2}, \quad \xi_R^0(g) = \frac{\mathcal{M}}{((1 - \Gamma_d)g + \mathcal{M}\Gamma_d)^2}. \tag{5.25}$$

This will be the initial condition for post-injection migration in the instantaneous-saturation limit.
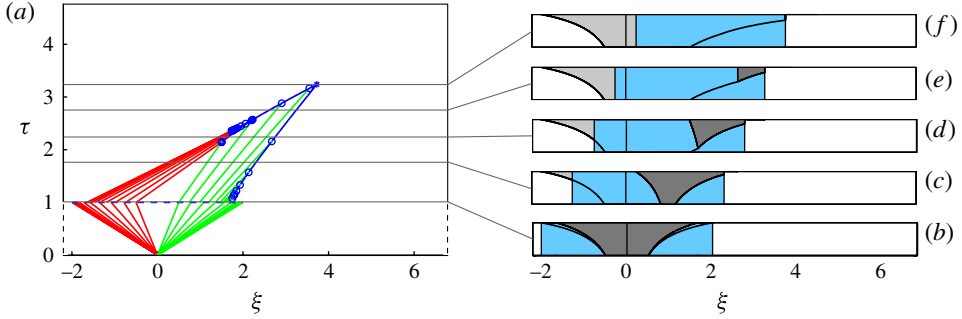
FIGURE 9. (Colour online) Post-injection migration in the instantaneous-saturation limit for case 2 of the flow-with-weak-slope interval, with $\mathcal{M} = 2$, $\Gamma = 0.5$, $N_f = 1$, $N_s = -0.75$, $S_{wc} = 0.4$, and $\Gamma_d = 0.1$. (*a*) The evolution of the plume in characteristic space with waves of the left and right fronts in dark grey (red online) and light grey (green online), respectively, and the paths of the peak, the shock, and the leading and trailing edges of the plume in solid black lines with open circles (blue online). (*b*)–(*f*) The shape of the plume at several times during migration, with mobile CO_2 in dark grey, the region containing residual CO_2 in light grey, the curtain of groundwater with dissolved CO_2 in mid grey (blue online), and groundwater in white. The curtain is approximate because we do not solve (4.2) in this limit. Note that the characteristics contract instantaneously across $\tau = 1$, where the characteristic time scale changes from the injection time scale to the post-injection time scale. This corresponds to the instantaneous saturation of the water beneath the end-of-injection plume shape (§ 5.4.1). Unlike in the slow-saturation limit, the characteristics here are straight lines. The leading edge of the plume is the instantaneous-saturation shock, which truncates the plume by cutting across characteristics. For comparison, both the characteristics and the plume shapes are drawn here on the same scale in space and time as those in figure 12 from Part 1 and figure 7 above. We include the injection period here, but denote that portion of the time axis ($\tau < 1$) with dashed lines to emphasize that the characteristic time scale may change dramatically from injection to post-injection, across $\tau = 1$ (§§ 4.1 and 4.2).

5.4.2. *Post-injection migration in the instantaneous-saturation limit*

The instantaneous velocity of each wave in this limit is again $G'/\widetilde{\mathcal{R}}$, with G' as given in (5.7). Because only the leading edge of the plume experiences solubility trapping in this limit, all other waves have constant thickness and therefore travel at constant speed. The value of $\widetilde{\mathcal{R}}$ is again determined by the sign of G'. Given the position of each wave at $\tau = 1$ and its instantaneous velocity in post-injection, we can write the position of each wave on the left and right fronts by integrating the velocity in time,

$$\xi_L = \xi_L^0(g) + \frac{1}{1-\Gamma}\left(-\left[\frac{N_s}{\mathcal{M}-1}\right] + \left[\mathcal{M}N_f + \frac{\mathcal{M}}{\mathcal{M}-1}N_s\right]\frac{1}{g^2}\right)(\tau-1), \quad (5.26a)$$

$$\xi_R = \xi_R^0(g) + \left(-\left[\frac{N_s}{\mathcal{M}-1}\right] + \left[\mathcal{M}N_f + \frac{\mathcal{M}}{\mathcal{M}-1}N_s\right]\frac{1}{g^2}\right)(\tau-1), \quad (5.26b)$$

The analysis then proceeds exactly as in Part 1 – waves collide, forming shocks or peaks, and we divide the analysis into parts based on the types of collisions that occur. For $-(\mathcal{M}-1) < N_s/N_f$, the left front compacts as it migrates. A shock will begin to

build from the leftmost point on the left front at time

$$\tau_\sigma^{LL} = 1 + \frac{(1 - \Gamma)(\mathcal{M} - 1)(1 - \Gamma_d)}{((\mathcal{M} - 1)N_f + N_s)((\mathcal{M} - 1)\Gamma_d + 1)^3}. \tag{5.27}$$

For $N_s/N_f < -(\mathcal{M} - 1)$, the right front compacts as it migrates. A shock will begin to build from the rightmost point on the right front at time

$$\tau_{RR}^\sigma = 1 - \frac{(\mathcal{M} - 1)(1 - \Gamma_d)}{((\mathcal{M} - 1)N_f + N_s)((\mathcal{M} - 1)\Gamma_d + 1)^3}. \tag{5.28}$$

For any value of N_s/N_f, the rightmost point on the left front and the leftmost point on the right front will collide at time

$$\tau_{LR}^{RL} = 1 + \frac{2(1 - \Gamma)}{\Gamma(N_f - N_s)}. \tag{5.29}$$

We must then divide the flow-with-weak-slope interval into cases based on the order in which these collisions occur. The possible cases here are again the same as in Part 1, but the delineation between them now depends on Γ_d in addition to $\mathcal{M}$, Γ, and N_s/N_f. Unlike in the slow-saturation limit, the comparison of collision times can be carried out explicitly for the first collision. For the collisions thereafter, however, the expressions are implicit and we therefore again implement a decision-tree algorithm to evaluate and compare these collision times, and evolve the plume accordingly. We describe in detail below the remainder of the development for case 2. First, we handle the propagation of the leading edge of the plume.

5.4.3. *Nose position in the instantaneous-saturation limit*

The leading edge of the plume dissolves rapidly in this limit, so we must handle its propagation separately. As the leading edge propagates to the right, it must lose enough mobile CO$_2$ to saturate the water that passes beneath. As a result, the plume is truncated at some moving position $x^\star$ where all of the CO$_2$ to the right of $x^\star$ has dissolved and all of the water to the left of $x^\star$ is saturated. By definition, then, $x^\star$ is the position across which there is no flux of CO$_2$. The volume flow rate of mobile CO$_2$ to the right at $x^\star$ can be written

$$F_g^\star(x^\star, t) = F_g(x^\star, t) - (1 - S_{wc})\phi h_1(x^\star, t)s_d, \tag{5.30}$$

where F_g is the total horizontal flow of CO$_2$ from (2.2) and $s_d = \mathrm{d}x^\star/\mathrm{d}t$. Similarly, the volume flow rate of water to the left at $x^\star$ can be written

$$F_w^\star(x^\star, t) = \phi h_w(x^\star, t)s_d - F_w(x^\star, t), \tag{5.31}$$

where F_w is the total horizontal flow of water from (2.7). The water flowing to the left must dissolve and carry away the entire amount $F_g^\star$ of CO$_2$ so that no mobile CO$_2$ crosses $\xi^\star$, and we therefore have that $F_g^\star = \chi_v F_w^\star$. Rearranging this expression gives

$$s_d = \frac{F_g + \chi_v F_w}{(1 - S_{wc})\phi h_1 + \chi_v \phi h_w}, \tag{5.32}$$

where the right-hand side is evaluated at $x^\star$. This is the speed of the instantaneous-saturation shock at the leading edge of the plume, given by the difference in the total flux of CO$_2$ across the shock divided by the difference in the total thickness of the CO$_2$ layer across the shock. Making s_d dimensionless and writing it in terms of g in

the hyperbolic limit, we have

$$\sigma_d = \frac{\chi_v(\mathscr{M}-1)N_f g + (1-\chi_v)(\mathscr{M}N_f(g-1) + N_s(\mathscr{M}-g)(g-1)/(\mathscr{M}-1))}{(1-\Gamma_d)(g-1)g + (\mathscr{M}-1)\Gamma_d g},$$

(5.33)

where σ_d is the dimensionless shock speed and the right-hand side is evaluated at $\xi^\star$. We can then formulate an ODE for the height of the shock as a function of time via the same construction used in (5.19), but where the shock speed is given by (5.33). This ODE is not separable for $\Gamma_d \neq 0$, so we integrate it numerically.

5.4.4. *Flow with weak slope, case 2, in the instantaneous-saturation limit*

In case 2, the first two collisions are the development of an incipient shock at the left, which occurs at time τ_{LL}^σ from (5.27), and the formation of a peak at the bottom, which occurs at time τ_{LR}^{RL} from (5.29). The ordering of these two collisions is unimportant. The initial height of the peak is $\mathscr{M}$, and the height of the peak as a function of time is given by the value of g at which ξ_L and ξ_R intersect, which yields a fourth-order polynomial in g. The height of the peak is the smallest root of this polynomial on the interval $g \in [1, \mathscr{M}]$. Meanwhile, the right front is truncated as the instantaneous-saturation shock evolves. The shock on the left evolves according to an ODE constructed as in (5.19), but where $\partial \xi / \partial g$ and $\partial \xi / \partial \tau$ are calculated using the expression for the shape of the left front from (5.26). The shock evolves until it collides with the peak, at which time the entire left front has become a shock. Thereafter, the shock collides continuously with the right front until it collides with the instantaneous-saturation shock at the leading edge of the plume. We plot the characteristics and plume shapes for case 2 in the instantaneous-saturation limit in figure 9.

6. Impact of solubility trapping on storage efficiency and migration speed

We now use the analysis of §5 to study the competition between capillary and solubility trapping, and the impact of solubility trapping on CO_2 migration.

Recall that we have chosen a characteristic time in post-injection migration based on groundwater flow so that $N_f \equiv 1$. We retain this choice here, but we report the results in this section in terms of the ratios N_s/N_f and N_d/N_f so that they remain valid for other choices of the characteristic time (§§ 4.2 and 5).

Further, recall that we have neglected the buoyant spreading term (the term proportional to N_g) in the analysis for simplicity (§ 5), because the macroscopic features of CO_2 migration and trapping are little affected by even large values of N_g compared to N_f or N_s (Hesse *et al.* 2008; Juanes & MacMinn 2008). All of the results reported here are therefore strictly valid for $N_g/N_f \to 0$.

As in Part 1, we interpret these results in the context of the storage efficiency, a macroscopic measure of CO_2 migration. The storage efficiency is the volume of CO_2 stored per unit pore volume of aquifer 'used', and is an important metric in capacity estimation (Bachu *et al.* 2007). We again define the storage efficiency ε as

$$\varepsilon = \frac{V_{CO_2}}{V_T} = \frac{Q_i T_i}{HL_T(1-S_{wc})\phi} = \frac{2}{\xi_T},$$

(6.1)

which is the ratio of the total volume of CO_2 injected, $Q_i T_i$, to the total pore volume available for CO_2 storage in a rectangle of thickness H and length L_T, where L_T is the total extent in the x-direction of the fully trapped CO_2 plume (Juanes &
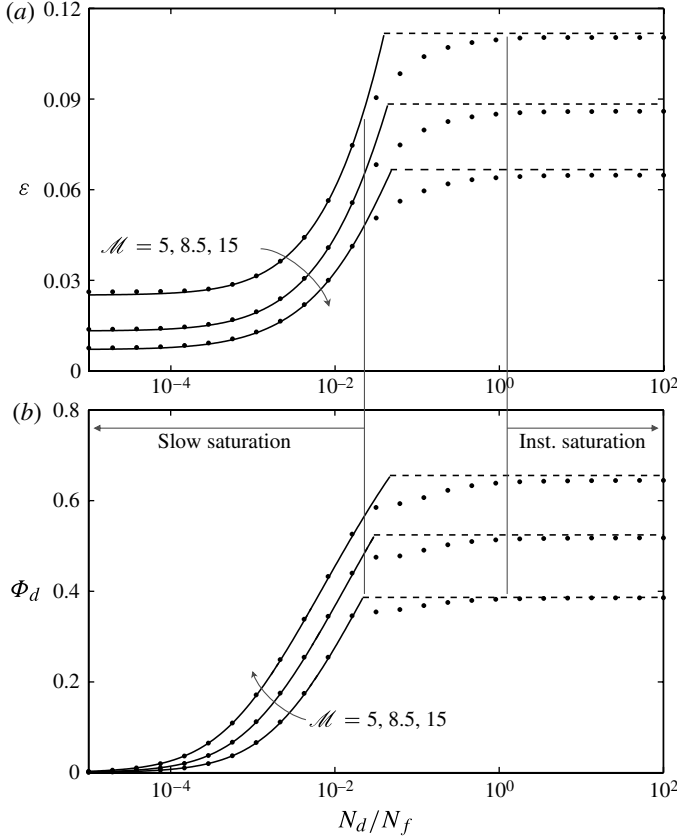
FIGURE 10. Both (*a*) the storage efficiency, ε, and (*b*) the fraction of CO$_2$ trapped by solubility trapping, Φ_d, increase monotonically with dimensionless rate of solubility trapping, N_d/N_f. Here, we fix the values of $\Gamma = 0.3$, $N_f = 1$, $N_s = -0.75$, $S_{wc} = 0.4$, and $\Gamma_d = 0.06$, and show curves for three typical values of $\mathcal{M}$, as indicated. Storage efficiency decreases monotonically with $\mathcal{M}$, as in Part 1, because the plume becomes longer and thinner as $\mathcal{M}$ increases; Φ_d increases monotonically with $\mathcal{M}$ because the amount of solubility trapping is proportional to the length of the plume. The water beneath the plume saturates more quickly as N_d increases, and both ε and Φ_d approach a plateau in the instantaneous-saturation limit where the water is completely saturated. The height of this plateau depends on Γ_d, but not on N_d. The semi-analytical solutions in the slow-saturation limit (solid black line) and the instantaneous-saturation limit (dashed black line) agree with numerical solutions to (4.1) and (4.2) (black dots) to within a few per cent.

MacMinn 2008; Juanes *et al.* 2010) and $\xi_T = L_T/L_c$. The storage efficiency is inversely proportional to the dimensionless footprint of residual CO$_2$, i.e. for a given volume of CO$_2$ injected, a larger footprint corresponds to less efficient storage.

We also consider an additional parameter here, which is the fraction Φ_d of CO$_2$ that has been trapped by solubility trapping once all of the CO$_2$ has been trapped. This is a measure of the importance of solubility trapping relative to capillary trapping since the remaining fraction $1 - \Phi_d$ must be trapped by capillarity.

Our focus in Part 1 was the competition between flow and slope, as measured by the ratio N_s/N_f. Here, we focus on the interactions between migration, capillary trapping, and solubility trapping. For this purpose, we fix N_s/N_f, Γ, Γ_d, and S_{wc}, and evaluate
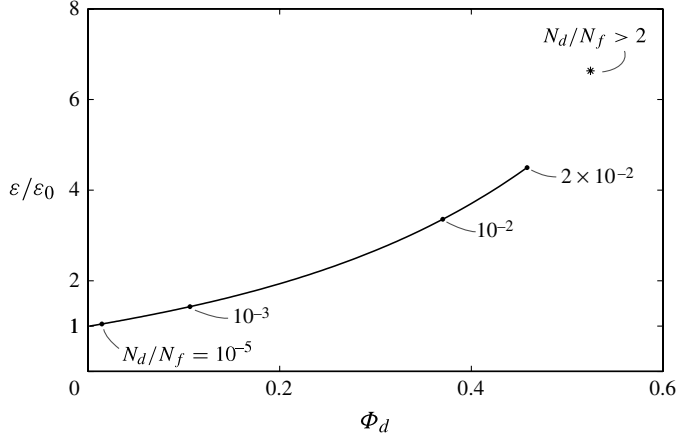
FIGURE 11. Solubility trapping can lead to a several-fold increase in storage efficiency even when the fraction trapped by solubility trapping is small. For $\mathcal{M} = 8.5$, we plot here the storage efficiency ε from figure 10(a), scaled by the storage efficiency without solubility trapping, ε_0, against the corresponding fraction trapped by solubility trapping Φ_d from figure 10(b). Both quantities increase monotonically with N_d/N_f (figure 10). Several values of N_d/N_f are indicated for reference (black dots). Results shown here are from the semi-analytical solutions for the limiting cases of slow saturation (solid black line) and instantaneous saturation (black star). The transition from slow to instantaneous saturation is not shown. The storage efficiency is twice the no-solubility-trapping value with only 20 % of the CO_2 trapped by solubility trapping, increasing in the instantaneous-saturation limit to ~ 6.6 times the no-solubility-trapping value with 52 % of the CO_2 trapped by solubility trapping.
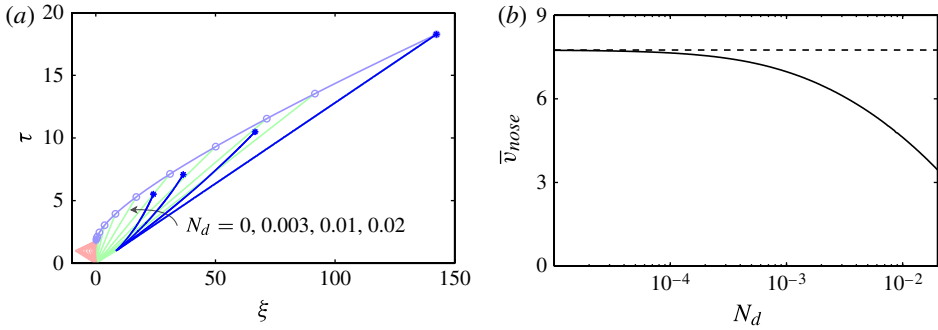

FIGURE 12. (Colour online) Solubility trapping reduces the speed at which the nose of the plume advances, as shown here in the slow-saturation regime for $\mathcal{M} = 8.5$, $\Gamma = 0.3$, $N_f = 1$, and $N_s = -0.75$. (a) In space–time, we superpose the path of the nose for several values of N_d (solid blue lines) onto the characteristics without solubility trapping (faded red, green, blue lines). Without solubility trapping ($N_d = 0$), the path of the nose is a straight line in space–time because the speed of the nose is constant (6.2). With solubility trapping, the nose travels more slowly and its path in space–time is curved because its speed is no longer constant (6.3). (b) The mean velocity of the nose (solid black line) decreases by more than a factor of 2 from its no-solubility-trapping value (dashed black line) as N_d increases from 0 to 0.02. For $N_d > 0.02$, plume migration is no longer in the slow-saturation limit for these parameters.
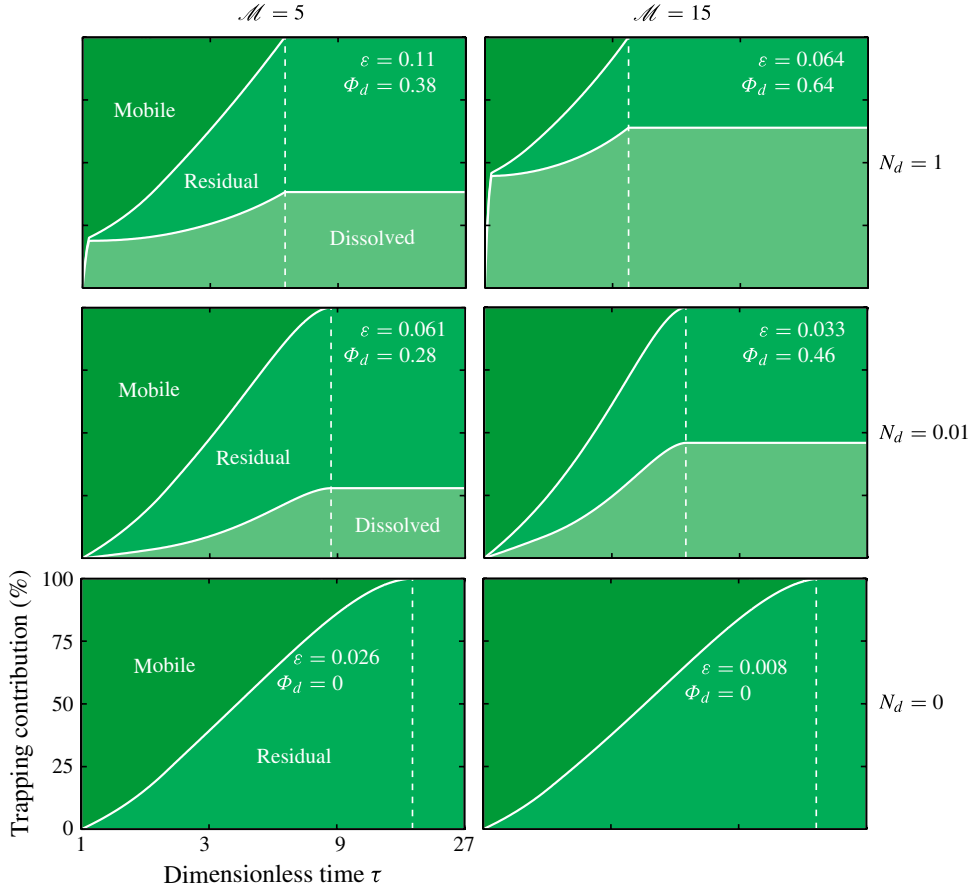
FIGURE 13. (Colour online) Solubility trapping is increasingly important as N_d increases, but capillary trapping plays an important role even for large N_d. Here, we show the time-evolution of the volume fractions of mobile, residual, and dissolved CO_2 for $N_d = 0$, 0.01, and 1 from bottom to top, respectively, and for $\mathcal{M} = 5$ (left) and 15 (right). The three volume fractions must add to 100 % at all times. Residual CO_2 does not dissolve in this model, so the fraction trapped by solubility trapping is constant once all of the CO_2 is trapped. We fix $\Gamma = 0.3$, $N_f = 1$, $N_s = -0.75$, $S_{wc} = 0.4$, $\Gamma_d = 0.06$. As N_d increases, the combination of capillary and solubility trapping traps the plume more quickly (total migration time decreases, as indicated here by the vertical, dashed, white lines), and over a shorter distance (storage efficiency increases). Note that in the instantaneous-saturation limit (top row), the amount of dissolved CO_2 increases sharply at $\tau = 1$ as the water beneath the end-of-injection plume saturates with dissolved CO_2; thereafter, solubility trapping occurs only at the leading edge (§ 5.4).

the storage efficiency and the fraction trapped by solubility trapping as a function of the ratio N_d/N_f for several values of $\mathcal{M}$.

Both the storage efficiency and the fraction trapped by solubility trapping increase monotonically with N_d/N_f (figure 10). However, storage efficiency decreases with $\mathcal{M}$ whereas fraction trapped by solubility trapping increases with $\mathcal{M}$. This is because the plume becomes longer and thinner as $\mathcal{M}$ increases, which slows capillary trapping but increases the amount of solubility trapping. In this sense, capillary and solubility trapping are complementary trapping mechanisms.

Comparing storage efficiency to the fraction trapped by solubility trapping at the same value of N_d/N_f, we find that the combination of capillary and solubility trapping can greatly increase storage efficiency even when the fraction trapped by solubility trapping is small (figure 11). This is a consequence of the complementary nature of capillary and solubility trapping: capillarity traps CO_2 at the short, trailing edge of the plume, while convective mixing acts most strongly along the long, leading edge.

In particular, solubility trapping slows the speed at which the leading edge advances, decreasing total migration distance and increasing the storage efficiency (6.1). Without solubility trapping, the dimensionless speed of the nose of the plume is constant ((3.4*d*) from Part 1):

$$v_{nose} = \mathrm{d}\xi_{RR}/\mathrm{d}\tau = \mathcal{M}N_f + N_s. \tag{6.2}$$

With solubility trapping, the speed of the nose in the slow-saturation limit can be evaluated from (5.11), and is given by

$$v_{nose}(\tau) = \frac{\mathcal{M}N_f + \mathcal{M}N_s/(\mathcal{M}-1)}{(1+(\mathcal{M}-1)N_d(\tau-1))^2} - \frac{N_s}{\mathcal{M}-1} - \frac{2\mathcal{M}(\mathcal{M}-1)N_d}{(1+(\mathcal{M}-1)N_d(\tau-1))^3}. \tag{6.3}$$

The speed of the nose is no longer constant in time, so the nose now traverses a curved path in space–time (figure 12*a*). In addition, the time-averaged speed of the nose decreases monotonically with N_d (figure 12*b*). Slowing the leading edge of the plume has a twofold impact on migration distance and therefore on storage efficiency: it decreases both migration speed and total migration time. Slowing the leading edge of the plume decreases total migration time because the plume of mobile CO_2 shrinks from the rear due to capillary trapping, becoming fully trapped when the trailing edge catches the leading edge. This occurs more quickly when solubility trapping slows the leading edge (figure 12*a*). Note that (6.3) is valid for all $N_s/N_f > -\mathcal{M}$, except for the narrow interval near $N_s/N_f = -\mathcal{M}$ where the leading edge of the plume is a shock (see Part 1, §§ 3.1.4 and 3.1.5); for $N_s/N_f < -\mathcal{M}$, the expression is identical except that the last term changes sign. The advancement of the nose in the instantaneous-saturation regime is more complicated because the leading edge is a shock, but the behaviour is qualitatively similar.

Because solubility trapping acts most strongly along the long, leading edge of the plume, capillary trapping remains important even for large values of N_d. We illustrate the complementary nature of capillary and solubility trapping via the time-evolution of the volume fractions of mobile, residual, and dissolved CO_2 (figure 13). This provides a quantitative, physical understanding of the time-evolution of the role of trapping mechanisms in immobilizing the buoyant CO_2, as recognized qualitatively in terms of perceived storage security in IPCC (2005, p. 208, figure 5.9).

7. Conclusions

In Part 1 of this series, we presented a complete solution to a theoretical model for the subsurface migration and capillary trapping of a plume of CO_2 in a confined, sloping aquifer with a natural groundwater through-flow. Here, we considered the impact of solubility trapping. We incorporated solubility trapping into the migration model, including the dissolution-limiting effect of the finite amount of water beneath the plume, and we identified two limiting cases in CO_2 migration with solubility trapping. We developed semi-analytical solutions to the migration equation in these limits, when the water beneath the plume saturates very slowly or very quickly ('instantaneously') relative to the motion of the plume. As in Part 1, we used these

solutions to explore the parameter space via the storage efficiency, a macroscopic measure of plume migration, and here also via the fraction of CO_2 that is ultimately trapped by solubility trapping.

We showed that capillary and solubility trapping are complementary trapping mechanisms because capillarity traps CO_2 at the short, trailing edge of the plume, while solubility trapping acts most strongly along the long, leading edge. Solubility trapping is most effective at large values of $\mathscr{M}$, when the plume is long and thin, and this is precisely when capillary trapping is least effective. We further showed that solubility trapping can lead to a several-fold increase in storage efficiency even when the fraction of CO_2 dissolved is small, because solubility trapping slows the speed at which the plume advances. However, capillary trapping plays an important role even when the rate of solubility trapping is large. As the rate of solubility trapping increases, the combination of the two mechanisms traps the plume more quickly (total migration time decreases), and over a shorter distance (storage efficiency increases). These results are useful for the insight they provide into the physics of CO_2 migration and trapping, and may also aid benchmarking and interpreting the predictions of more complicated numerical models.

We have derived and studied a simple but physics-based model and, in doing so, we have made many simplifying assumptions. For example, our analysis is planar, assuming line-symmetry and neglecting lateral flow. This assumption is justified by the injection scenario we consider, injection at the scale of a geologic basin via a line-drive array of wells. However, three-dimensional flow may become important at later times as the plume migrates sufficiently far from the injection wells, or if the direction of groundwater flow is not completely aligned with the slope. We have also assumed that the thickness of the aquifer is uniform and that the caprock is flat: in practice, this is rarely the case. These effects are not included here, but can be accounted for in a computational framework (Gasda, Nordbotten & Celia 2009; Gasda *et al.* 2011).

We have not included leakage here; however, the CO_2 plume will probably encounter faults or fractures in the caprock as it migrates because its areal footprint will be very large. Capillary entry pressure will inhibit leakage in many cases, but the impact of leakage will ultimately be very sensitive to the distribution and permeability of the leakage pathways (Pritchard 2007; Farcas & Woods 2009; Neufeld *et al.* 2009; Woods & Farcas 2009).

Further, although we have assumed that the aquifer is homogeneous, all natural rocks are heterogeneous at some scale. The impact of heterogeneity on CO_2 migration and trapping is not well understood, but it will depend strongly on the nature, scale, and distribution of the heterogeneity.

These considerations are beyond the scope of this study, but they will have some quantitative bearing on the results presented here. However, it is unlikely that they will have a strong qualitative impact on the fundamental nature of the interaction between slope and groundwater flow, or the competition between capillary and solubility trapping.

REFERENCES

BACHU, S. 2003 Screening and ranking of sedimentary basins for sequestration of CO_2 in geological media in response to climate change. *Environ. Geol.* **44** (3), 277–289.

BACHU, S., BONIJOLY, D., BRADSHAW, J., BURRUSS, R., HOLLOWAY, S., CHRISTENSEN, N. P. & MATHIASSEN, O. M. 2007 CO_2 storage capacity estimation: methodology and gaps. *Intl J. Greenh. Gas Control* **1** (4), 430–443.

BACHU, S., GUNTER, W. D. & PERKINS, E. H. 1994 Aquifer disposal of CO_2: hydrodynamic and mineral trapping. *Energy Convers. Manage.* **35** (4), 269–279.

BACKHAUS, S., TURITSYN, K. & ECKE, R. E. 2011 Convective instability and mass transport of diffusion layers in a Hele–Shaw geometry. *Phys. Rev. Lett.* **106** (10), 104501.

BEAR, J. 1972 *Dynamics of Fluids in Porous Media*. Elsevier, reprinted with corrections by Dover, 1988.

BICKLE, M., CHADWICK, A., HUPPERT, H. E., HALLWORTH, M. & LYLE, S. 2007 Modelling carbon dioxide accumulation at Sleipner: implications for underground carbon storage. *Earth Planet. Sci. Lett.* **255** (1–2), 164–176.

CARBON CAPTURE AND SEQUESTRATION TECHNOLOGIES @ MIT 2010 CO_2 thermophysical property calculator. URL: http://sequestration.mit.edu/tools/index.html.

DUAN, Z. & SUN, R. 2003 An improved model calculating CO_2 solubility in pure water and aqueous NaCl solutions from 273 to 533 K and from 0 to 2000 bar. *Chem. Geol.* **193** (3–4), 257–271.

ELDER, J. W. 1968 The unstable thermal interface. *J. Fluid Mech.* **32** (1), 69–96.

ENNIS-KING, J. & PATERSON, L. 2005 Role of convective mixing in the long-term storage of carbon dioxide in deep saline formations. *SPE J.* **10** (3), 349–356.

ENNIS-KING, J., PRESTON, I. & PATERSON, L. 2005 Onset of convection in anisotropic porous media subject to a rapid change in boundary conditions. *Phys. Fluids* **17**, 084107.

FARCAS, A. & WOODS, A. W. 2009 The effect of drainage on the capillary retention of CO_2 in a layered permeable rock. *J. Fluid Mech.* **618**, 349–359.

GARCÍA, J. 2001 Density of aqueous solutions of CO_2. Lawrence Berkeley National Laboratory: Lawrence Berkeley National Laboratory, retrieved from: http://www.escholarship.org/uc/item/6dn022hb.

GARVEN, G. 1995 Continental-scale groundwater flow and geologic processes. *Annu. Rev. Earth Planet. Sci.* **23**, 89–117.

GASDA, S. E., NORDBOTTEN, J. M. & CELIA, M. A. 2009 Vertical equilibrium with sub-scale analytical methods for geological CO_2 sequestration. *Comput. Geosci.* **79** (1), 15–27.

GASDA, S. E., NORDBOTTEN, J. M. & CELIA, M. A. 2011 Vertically-averaged approaches for CO_2 migration with solubility trapping. *Water Resour. Res.* **47**, W05528.

GUNN, I. & WOODS, A. W. 2011 On the flow of buoyant fluid injected into a confined, inclined aquifer. *J. Fluid Mech.* **672**, 109–129.

HESSE, M. A., ORR, F. M. JR & TCHELEPI, H. A. 2008 Gravity currents with residual trapping. *J. Fluid Mech.* **611**, 35–60.

HESSE, M. A., TCHELEPI, H. A., CANTWELL, B. J. & ORR, F. M. JR 2007 Gravity currents in horizontal porous layers: transition from early to late self-similarity. *J. Fluid Mech.* **577**, 363–383.

HESSE, M. A., TCHELEPI, H. A. & ORR, F. M. JR 2006 Scaling analysis of the migration of CO_2 in saline aquifers. In *SPE Annual Technical Conference and Exhibition, San Antonio, TX (SPE 102796)*.

HIDALGO, J. & CARRERA, J. 2009 Effect of dispersion on the onset of convection during CO_2 sequestration. *J. Fluid Mech.* **640**, 441–452.

HUPPERT, H. E. & WOODS, A. W. 1995 Gravity-driven flows in porous layers. *J. Fluid Mech.* **292**, 55–69.

IPCC 2005 Carbon dioxide capture and storage. *Special report prepared by Working Group III of the Intergovernmental Panel on Climate Change, Cambridge, UK*.

JUANES, R. & MACMINN, C. W. 2008 Upscaling of capillary trapping under gravity override: application to CO_2 sequestration in aquifers. In *SPE/DOE Symposium on Improved Oil Recovery, Tulsa, OK, USA (SPE 113496)*.

JUANES, R., MACMINN, C. W. & SZULCZEWSKI, M. L. 2010 The footprint of the CO_2 plume during carbon dioxide storage in saline aquifers: storage efficiency for capillary trapping at the basin scale. *Trans. Porous Med.* **82** (1), 19–30.

JUANES, R., SPITERI, E. J., ORR, F. M. JR & BLUNT, M. J. 2006 Impact of relative permeability hysteresis on geological CO_2 storage. *Water Resour. Res.* **42**, W12418.

KHARAKA, Y. K. & HANOR, J. S. 2003 Deep fluids in the continents. Part I. Sedimentary basins. In *Treatise on Geochemistry*, vol. 5. pp. 1–48. Elsevier.

KNEAFSEY, T. J. & PRUESS, K. 2010 Laboratory flow experiments for visualizing carbon dioxide-induced, density-driven brine convection. *Trans. Porous Med.* **82** (1), 123–139.

KOCHINA, I. N., MIKHAILOV, N. N. & FILINOV, M. V. 1983 Groundwater mound damping. *Intl J. Engng Sci.* **21** (4), 413–421.

LACKNER, K. S. 2003 Climate change: a guide to CO_2 sequestration. *Science* **300** (5626), 1677–1678.

LAX, P. D. 1972 The formation and decay of shock waves. *Am. Math. Mon.* **79** (3), 227–241.

LINDEBERG, E. & WESSEL-BERG, D. 1997 Vertical convection in an aquifer column under a gas cap of CO_2. *Energy Convers. Manage.* **38**, S229–S234.

MACMINN, C. W. & JUANES, R. 2009 Post-injection spreading and trapping of CO_2 in saline aquifers: impact of the plume shape at the end of injection. *Comput. Geosci.* **13** (4), 483–491.

MACMINN, C. W., SZULCZEWSKI, M. L. & JUANES, R. 2010 CO_2 migration in saline aquifers. Part 1. Capillary trapping under slope and groundwater flow. *J. Fluid Mech.* **662**, 329–351.

NEUFELD, J. A., HESSE, M. A., RIAZ, A., HALLWORTH, M. A., TCHELEPI, H. A. & HUPPERT, H. E. 2010 Convective dissolution of carbon dioxide in saline aquifers. *Geophys. Res. Lett.* **37**, L22404.

NEUFELD, J. A., VELLA, D. & HUPPERT, H. E. 2009 The effect of a fissure on storage in a porous medium. *J. Fluid Mech.* **639**, 239–259.

NICOT, J. -P. 2008 Evaluation of large-scale CO_2 storage on fresh-water sections of aquifers: an example from the Texas Gulf Coast Basin. *Intl J. Greenh. Gas Control* **2** (4), 582–593.

NORDBOTTEN, J. M. & CELIA, M. A. 2006 Similarity solutions for fluid injection into confined aquifers. *J. Fluid Mech.* **561**, 307–327.

ORR, F. M. JR 2009 Onshore geologic storage of CO_2. *Science* **325** (5948), 1656–1658.

PAU, G. S. H., BELL, J. B., PRUESS, K., ALMGREN, A. S., LIJEWSKI, M. J. & ZHANG, K. 2010 High-resolution simulation and characterization of density-driven flow in CO_2 storage in saline aquifers. *Adv. Water Resour.* **33** (4), 443–455.

PRITCHARD, D. 2007 Gravity currents over fractured substrates in a porous medium. *J. Fluid Mech.* **584**, 415–431.

RAPAKA, S., CHEN, S., PAWAR, R. J., STAUFFER, P. H. & ZHANG, D. 2008 Non-modal growth of perturbations in density-driven convection in porous media. *J. Fluid Mech.* **609**, 285–303.

RAPAKA, S., PAWAR, R. J., STAUFFER, P. H., ZHANG, D. & CHEN, S. 2009 Onset of convection over a transient base-state in anisotropic and layered porous media. *J. Fluid Mech.* **614**, 227–244.

RIAZ, A., HESSE, M., TCHELEPI, H. A. & ORR, F. M. JR 2006 Onset of convection in a gravitationally unstable diffusive boundary layer in porous media. *J. Fluid Mech.* **548**, 87–111.

SCHRAG, D. P. 2007 Preparing to capture carbon. *Science* **315** (5813), 812–813.

SLIM, A. C. & RAMAKRISHNAN, T. S. 2010 Onset and cessation of time-dependent, dissolution-driven convection in porous media. *Phys. Fluids* **22** (12), 124103.

VERDON, J. & WOODS, A. W. 2007 Gravity-driven reacting flows in a confined porous aquifer. *J. Fluid Mech.* **588**, 29–41.

WEIR, G. J., WHITE, S. P. & KISSLING, W. M. 1996 Reservoir storage and containment of greenhouse gases. *Trans. Porous Med.* **23** (1), 37–60.

WOODING, R. A., TYLER, S. W. & WHITE, I. 1997a Convection in groundwater below an evaporating salt lake. Part 1. Onset of instability. *Water Resour. Res.* **33** (6), 1199–1217.

WOODING, R. A., TYLER, S. W., WHITE, I. & ANDERSON, P. A. 1997b Convection in groundwater below an evaporating salt lake. Part 2. Evolution of fingers or plumes. *Water Resour. Res.* **33** (6), 1219–1228.

WOODS, A. W. & FARCAS, A. 2009 Capillary entry pressure and the leakage of gravity currents through a sloping layered permeable rock. *J. Fluid Mech.* **618**, 361–379.